



Bachelor of Science Thesis

Joint Degree Program in Geosciences
Ludwig-Maximilians-Universität München
and
Technische Universität München

The 2017 Intraplate Earthquake in Botswana: Computational Modeling of the Rupture Dynamics

Chair of Geophysics
Department of Earth and Environmental Sciences
Ludwig-Maximilians-Universität München
Theresienstraße 41
80333 München

Written by: Sophia Gahr
Matriculation Number LMU: 11700061
Matriculation Number TUM: 03693946
Submission Date: May 3, 2021
Supervised by: Prof. Dr. Alice-Agnes Gabriel
Dr. Max Moorkamp

Acknowledgements

First of all, I would like to thank my supervisors Alice and Max for the opportunity to study such a fascinating natural phenomenon. Through your guidance in a weekly meeting I was able to gain first experiences in research and scientific working. Special thanks goes to Thomas Ulrich for helping me in understanding large Python codes and for submitting simulation jobs on SuperMUC. Further thanks goes to Aniko Wirp for helping out in any kind of questions. A big thank you goes to Jens Oeser for the setup of IT infrastructures. Then, I would like to thank my fellow students Janina and Katharina. You have accompanied me throughout my bachelor studies and now I'm curious where the journey will take us. I thank Sebastian for his precious help in script automation. You saved me quite some time. I thank my parents for supporting me in my decisions and always giving me valuable advice and support. Last but not least, I thank my dear brother for his programming skills and English expertise – I owe you a cake.

Abstract

Intraplate earthquakes can be devastating and are unpredictable as they often occur on previously unknown faults. They imply a great danger to both human lives and infrastructures since adequate concepts for hazard calculation in intraplate regions do not exist. Up to now, their origin and genesis are still broadly discussed in geophysics. The 2017 intraplate earthquake near Mojabana in Botswana provides a unique opportunity to study the mechanisms that lead to such events as detailed geophysical data are available. This thesis evaluates a fault plane solution for this large event. We perform static analysis on the inferred fault plane to ascertain its stress state. To pursue this objective, we constrain the parameter space of four quantities that control the state of stress of the fault. Moreover, we analyze the influence of different fault geometries on the fault's static strength. In order to verify our findings, we run dynamic rupture simulations. The results confirm previous assumptions, namely the unsuitability of the inferred fault plane to host a large earthquake as it was observed in Botswana. Therefore, no indications regarding a trigger mechanism of the Mojabana earthquake were obtained.

Contents

Acknowledgements	iii
Abstract	v
1 Introduction on intraplate Earthquakes	1
2 The Botswana intraplate Earthquake on 3 April 2017	5
2.1 State of Knowledge	5
2.2 Tectonic Setting	9
2.3 Trigger Hypothesis	10
3 Static Analysis of the Fault Plane	13
3.1 Methodical Approach of the static Analysis	13
3.2 Fault Geometry	14
3.3 Investigation of the Stress State	18
3.3.1 Relative Prestress Ratio and Parameters	18
3.3.2 The Stress Shape Ratio	20
3.3.3 The Fluid Pressure Ratio	20
3.3.4 The initial relative Prestress Ratio	22
3.3.5 The Azimuth of maximum horizontal compressive Stress .	23
3.4 Results and Discussion	24
3.4.1 Constrained Parameters	24
3.4.2 Evaluation of different Fault Geometries	27
4 Simulation of the Rupture Dynamics	31
4.1 Methodical Approach of the dynamic Rupture	31
4.2 Dynamic Rupture modeling Setup	32
4.2.1 Mesh Generation	32
4.2.2 Input Files	32

Contents

4.3 Results and Discussion	34
4.3.1 First Simulation	34
4.3.2 Second Simulation	35
5 Conclusion and Outlook	39
List of Figures	43
List of Tables	45
Bibliography	47
Statement of Authorship	55

1 Introduction on intraplate Earthquakes

As most of the seismic activity happens at plate margins, earthquakes within lithospheric plates far from active plate boundaries represent a minority in seismic energy release. Intraplate earthquakes are often devastating since they are unpredictable and the attenuation of seismic energy within plate interiors is low [Hanks & Johnston, 1992]. As such, they pose a great danger to both human lives and infrastructures. Aggravating the threat, affected regions often are ill prepared and appropriate measures to prevent earthquake damages have not been taken. Additionally, adequate concepts for hazard calculation in intraplate regions do not exist. Hazard calculation gets more challenging since instrumentally recorded large intraplate events are quite rare and opportunities to study them are limited. There is evidence that seismicity may be triggered by anthropogenic activity, e. g. fluid or wastewater injections during oil recovery or mining processes and the filling of water reservoirs [Keranen et al., 2014; Gupta, 1985]. Fluid overpressure as result of uprising volatiles from the mantle is assumed to cause earthquakes [Cappa et al., 2009]. Further, surface load variations can lead to rupture in the lithosphere as confirmed by studies from e. g. Heki [2003], Hetzel and Hampel [2005], Bettinelli et al. [2008], Turpeinen et al. [2008], Calais et al. [2010], and González et al. [2012], respectively. They correlate monsoon rains, lake regression, water extraction from an aquifer, snow loading, the melting of ice sheets or glaciers, and erosional events with seismicity.

Historically, there were relatively few large intraplate earthquakes with magnitudes $M > 6$. Figure 1 highlights their global occurrences up to 2016. Most of these events happened in stable continental regions (SCR). Johnston [1989] defines those as "areas where the continental crust is largely unaffected by currently active plate boundaries". Examples for earthquakes in SCR are the 1811-1812

1 Introduction on intraplate Earthquakes

New Madrid events in the Central U. S. with moment magnitudes $M_W \geq 7$ [Hough et al., 2000], the 1988 Tennant Creek earthquakes ($M_W \geq 6$) in Australia [Bowman, 1992], the Bhuj earthquake ($M_W 7.7$) in India [Calais et al., 2016] or the series of earthquakes in western Europe such as the Basel (1356), the Lisbon (1755) or the Nice (1887) events [see Calais et al., 2016]. In 2012, the largest intraplate strike-slip event ($M_W 8.6$) in known history occurred in the Indian Ocean [Yadav et al., 2013]. Most recently, the 2017 Botswana event ($M_W 6.5$) happened in southern Africa. This large earthquake is studied in this thesis.

Earthquakes far from plate boundaries can also occur within stable oceanic regions (white in red circles in Figure 1). Notably, they happen less numerous. This could be due to the higher homogeneity of oceanic crust compared to continental crust, as the age of oceanic crust never exceeds 200 Ma [Calais et al., 2016].

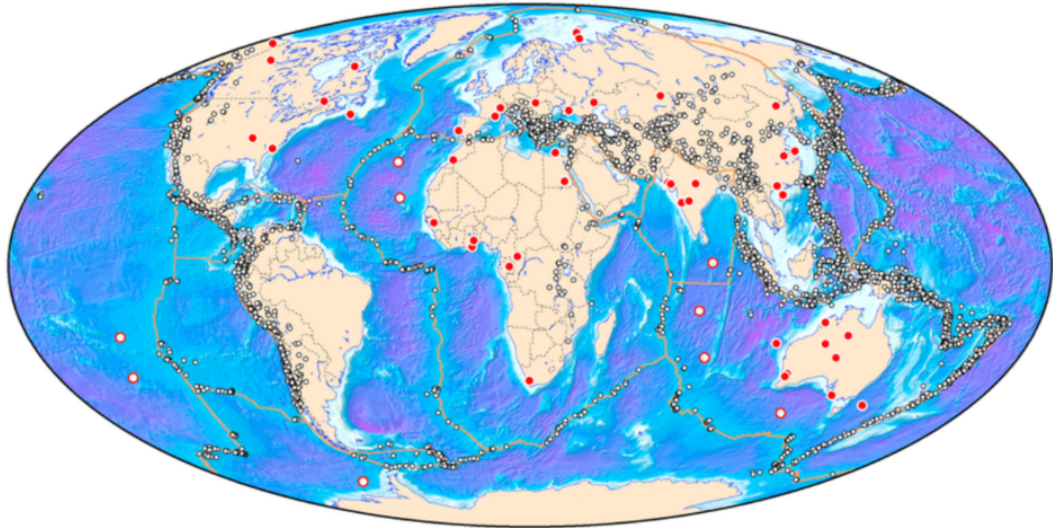


Figure 1: Worldwide seismic activity of intraplate earthquakes. The map shows the worldwide distribution of large intraplate earthquakes ($M > 6$) up to 2016. Red dots are events in stable continental regions, while white in red circles mark earthquakes in stable oceanic regions. Plate boundaries are outlined in gray. Source: U.S. Geological Survey [2021], modified.

Intraplate earthquakes can be clustered in time as a series of multiple events with long periods of quiescence (100 000 years and more [Clark et al., 2012]), while others appear to have ruptured only once in a single event. Paleo-seismological

data allow the observation that intraplate earthquakes appear not to repeat on the same fault [see Talwani, 2017, and references herein], which may be a striking feature of intraplate earthquakes. Consequently, hazard calculation for intraplate regions is challenging as intraplate earthquakes occur infrequent and often happen on previously unknown faults with great spatial uncertainties. On the one hand, concepts for hazard calculations have been developed for plate boundaries, and on the other hand, knowledge about the nature of intraplate earthquakes is still deficient [Calais et al., 2016]. Therefore, these concepts should be applied with care within stable continental regions.

A first attempt to explain intraplate earthquakes was made by Sykes in 1978. He describes that they preferably occur along preexisting zones of weakness in the continental crust. Based on further investigations with improved seismicity and geodetic data, the study of Mazzotti [2007] supports the weak zone approach. In 2014, Talwani introduced a unified model for intraplate earthquakes. He aims to explain previously observed features of intraplate events and to integrate them with newer ones. His model describes geological structures that act as *local* stress concentrators (LSC) with wavelengths of tens to hundreds of kilometers. This view contrasts previous models that explain intraplate seismicity with *regional* stress concentrators based on weak zones. These LSC include mafic plutonic intrusions [Long, 1976], rift pillows [Zoback & Richardson, 1996], intersecting faults [Talwani, 1988], and restraining stepovers [Talwani, 2014]. Globally, the vast amount of the seismic energy release in SCR is related to old rift structures [Talwani, 2014] and, less numerous, to the edges of cratons [Mooney et al., 2012]. According to Talwani's unified model, the crust eventually ruptures into an earthquake, when the magnitude of the local stress field in any LSC becomes the same order of magnitude as the regional stress field. Talwani concludes that local stress perturbations are rather the cause of seismicity than smaller surface load variations through e. g. deglaciation and erosion, as listed above. Besides this, accumulated stresses in LSC can locally rotate the direction of the regional stress field [Zoback, 1992]. The regional stress field is generated by tectonic forces at plate boundaries and extends over thousands of kilometers [Calais et al., 2016]. Directions for its compressional stresses can be extracted from the World Stress Map [see Heidbach et al., 2016a].

1 Introduction on intraplate Earthquakes

In 2016, however, Calais et al. challenged the unified model. They state that LSC persist temporally, whereas intraplate seismicity is transient and faults seem to rupture only once. These local stress concentrators therefore are insufficient in explaining the episodic occurrence of large intraplate earthquakes. The authors rather propose a trigger mechanism via transient stress changes, such as surface load variations or fluid diffusion in the crust. According to Calais et al., these small variations in the stress field suffice as the faults are at failure equilibrium. Moreover, the authors state that large-scale stress changes in the regional stress field occur at very low rates. This can be observed by strain measurements in plate interiors. The New Madrid Seismic Zone for instance shows large earthquakes in the last 3000 years, while no detectable strain buildup was observed (less than $0.2 \frac{\text{mm}}{\text{a}}$ over 100 km). This contradicts the fact that strain energy locally accumulates over short timescales (~ 1000 years). The strain energy is then released in large intraplate earthquakes.

This thesis focuses on the 2017 intraplate earthquake in Botswana. Chapter 2 will summarize this event and provide background information on the tectonic setting in Botswana. Furthermore, previously proposed trigger mechanisms are presented. In chapter 3, we evaluate a fault plane solution for this earthquake because its origin is still unknown. Our findings are based on detailed geophysical data. To pursue the investigation, chapter 4 verifies the constrained fault geometry as well as the fault's state of stress in a simulation of the rupture dynamics. Typically, the Global Centroid Moment Tensor provides two admissible fault plane solutions for the earthquake. The thesis "Mechanisms of intraplate earthquakes: The 2017 Botswana event" from Obermaier [2020] elaborated a first solution. In this thesis however, we focus on a second fault plane solution. We infer our results from the same data sets upon which Obermaier based his findings. With this approach, we try to confirm (or refute) earlier proposed trigger mechanisms as large uncertainties and discrepancies still remain. In general, we aim to gain new insights in the so far poorly understood intraplate earthquakes.

2 The Botswana intraplate Earthquake on 3 April 2017

2.1 State of Knowledge

On 3 April 2017, a M_W 6.5 earthquake happened in central Botswana, southern Africa. According to the U.S. Geological Survey (USGS), the epicenter was located at -22.678° latitude and 25.156° longitude. The map in Figure 2 shows Botswana in southern Africa. The yellow star marks the epicenter, ~ 132 km west of the city Mojabana. The earthquake, hereinafter referred to as Mojabana earthquake, occurred in the lower crust, in a depth greater than 20 km [Kolawole et al., 2017]. Its underlying focal mechanism was normal faulting, which is consistent with extensional stress patterns in southern Africa [see World Stress Map, Heidbach et al., 2016a]. Due to its location far from any known plate boundaries (the nearest seismically active zone is > 300 km to the northwest, see section 2.2), the earthquake is classified as intraplate earthquake. The Mojabana event is the largest intraplate earthquake in the last 30 years [Fadel et al., 2020] and the second largest earthquake in Botswana's recorded history since the M_W 6.7 event in 1952 in the Okavango Delta region [Modisi et al., 2000]. In general, Botswana is characterized by a low-level seismicity [Pagani et al., 2018]. The earthquake was felt throughout southern Africa, although little damage was reported as the epicenter was remote from populated areas [Midzi et al., 2018].

Several studies provide a fault plane solution for the Mojabana earthquake. The modeled source parameter vary in strike, dip and rake angle, specify the hypocentral depth, and some also examine the amount of slip. Kolawole et al. [2017] find a northwest-southeast striking and northeast dipping normal fault at a dip angle of 53° . This observation coincides with nodal plane 1 of the USGS solution.

2 The Botswana intraplate Earthquake on 3 April 2017

However, the deep source of the earthquake and the proximity of the fault trace to the earthquake epicenter suggest a steep dipping angle between $72\text{--}74^\circ$ (Table 1). They explain these findings with a listric fault, shallowing the dip angle in depth. In their study, the authors use a rake angle of -114° and obtain a slip of 1.8 m in a depth at 21–24 km.

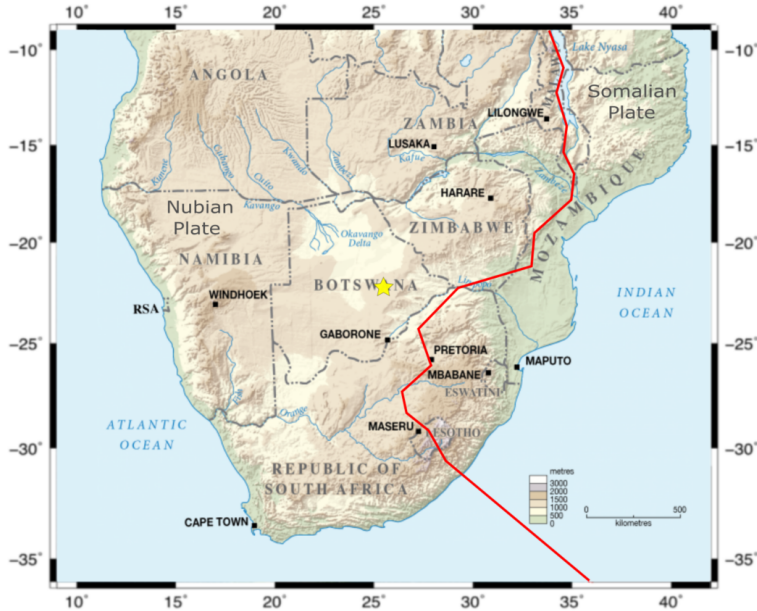


Figure 2: Map of southern Africa. The epicenter of the Mojabana earthquake (yellow star) is located in Botswana, southern Africa. Red lines show the boundary of the East African Rift System after Bird [2003]. The coordinate axes are in degree longitude and degree latitude. North points to the top. Source: CartoGIS Services et al. [2021], modified.

The authors Albano et al. [2017] confirm the NW-SE fault orientation with a best-fitting dip angle of 65° . They obtain a bigger slip of 2.7 m and a rake angle of -131° , however. These differences can be explained knowing that Kolawole et al. fixed the rake angle during the inversion of Interferometric Synthetic Aperture Radar (InSAR) data while Albano et al. allowed a variation of the angle.

Fitting their observation best, Gardonio et al. [2018] find a NW-SE striking fault plane with a dip angle of 73° to the northeast, whereas Materna et al. [2019] find a strike of 126° . Unlike the previous studies, Materna et al. choose a dip direction to the southwest with an angle of 51° . It has to be noted that both Gardonio et al. and Materna et al. claim fault planes close to either USGS focal mechanism nodal plane are able to satisfy the observations. They cannot confirm

2.1 State of Knowledge

with certainty that the earthquake happened on the northeast dipping fault or on the southwest dipping fault, respectively, as both fault geometries in each study explain the findings well. Materna et al. [2019] resolve this ambiguity with the inversion of InSAR and teleseismic data, choosing the northwest striking and southwest dipping fault as causative fault plane. In contrast to both Kolawole et al. [2017] and Albano et al. [2017], Materna et al. use the Global Centroid Moment Tensor rake angle (-107°), which may contribute to differences in the results as they obtain a smaller slip (0.66 m). Different fault geometries may also lead to resulting disparities in slip.

Table 1: Fault plane parameters. The table lists parameters for strike, dip and rake, as well as the obtained slip in meter and the depth of the hypocenter in kilometer for various studies.

Paper	Strike [°]	Dip [°]	Rake [°]	Slip [m]	Depth [km]
Kolawole et al.	126 NW-SE	72-74 NE	-114	1,8	21-24
Albano et al.	304 NW-SE	65 NE	-131	2,7	> 20
Gardonio et al.	NW-SE	73 NE	-	-	29
Materna et al.	126 NW-SE	51 SW	-107	0,66	29

All authors verify the location of the hypocenter in a depth greater than 20 km. Kolawole et al. [2017] suggest a depth of 21–24 km, whereas both Gardonio et al. [2018] and Materna et al. [2019] place the earthquake well into the lower crust at 29 km (Table 1). Most authors [e. g. Kolawole et al.; Albano et al.; Gardonio et al.] agree on a magnitude M_W 6.5 as provided by the USGS. Only Materna et al. favor a slightly smaller magnitude (M_W 6.4), based on their InSAR data analysis and inversion results. They explain the difference with a higher-than-average shear modulus at the hypocenter, leading to a slightly smaller moment magnitude.

Two sequences of foreshocks with magnitudes smaller than 4 proceeded the Botswana earthquake [Olebetse et al., 2020]. In total, the authors identified nine foreshocks. They are randomly distributed across the country [see figure 4 in Olebetse et al., 2020] with exception of the southwestern part of Botswana where no event was recorded. The first foreshocks associated with the Mojabana event occurred between December 2016 and early January 2017. Following a seismically quiet period with a single small event (local magnitude M_L 1.8) in

2 The Botswana intraplate Earthquake on 3 April 2017

February, the second sequence started in March 2017, lasting until 2 weeks before the main event [Olebetse et al., 2020].

The main event on 3 April 2017 was followed by about 21 smaller events with the largest local magnitude M_L 5.3 [Olebetse et al., 2020]. The last aftershock occurred on 12 August 2017 [Moorkamp et al., 2019]. Figure 3 gives an overview on the seismicity of Botswana from April 2017 to March 2018. Most events are clustered around the mainshock. The farthest aftershocks occurred ~ 240 km away from the main event [Olebetse et al., 2020]. The aftershocks indicate a northwest-southeast trend [Midzi et al., 2018] which is consistent with fault plane solutions [e. g. Kolawole et al., 2017; Albano et al., 2017; Gardonio et al., 2018; Materna et al., 2019; Table 1] for the Mojabana event. Both fore- and aftershock activity happened at shallower depths than the main event [Olebetse et al., 2020].

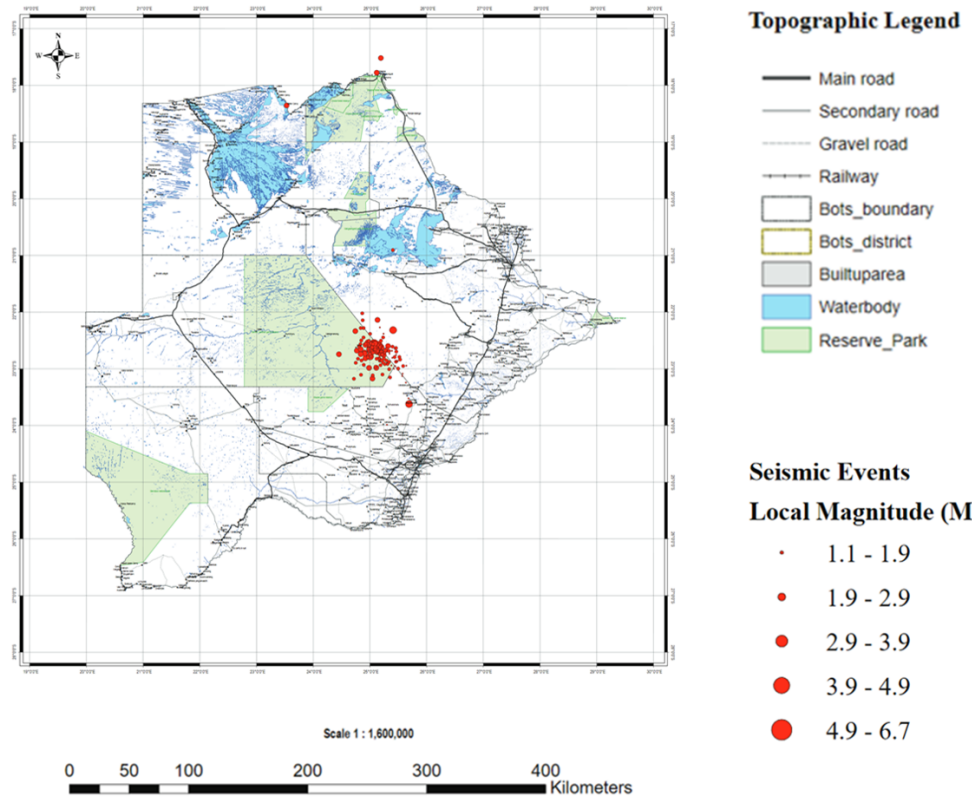


Figure 3: Seismicity of Botswana. The Map shows the seismicity of Botswana following the main event, lasting until March 2018. Most aftershocks (red dots) are clustered around the main shock. Source: Botswana Geoscience Institute [2018], modified.

2.2 Tectonic Setting

Tectonics in southern Africa are predominantly characterized by the East African Rift System (EARS). Its simplified boundaries are shown in red in Figure 2. As the continent is slowly drifting apart in approximately east-west direction, normal faulting earthquakes are promoted. The Somalian Plate is moving eastward with respect to the Nubian Plate at $6.5 \frac{\text{mm}}{\text{a}}$ in the northern part, slowing down to less than $2 \frac{\text{mm}}{\text{a}}$ in the southern part of the EARS [Stamps et al., 2008].

The state of Botswana is located centrally in southern Africa. It consists of old Archean cratons and several younger Proterozoic orogenic belts. Figure 4 depicts the tectonic units in Botswana. We find the Congo Craton in the northwest and the Kalahari Craton in the south and east. The Kalahari Craton was formed by the collision of the Zimbabwe and Kaapvaal Cratons, 2700 – 2500 Ma ago [Fadel et al., 2020]. Later, the Limpopo Belt emerged in the Paleoproterozoic (2500 – 1600 Ma). In the following period, it grew larger and formed both the Magondi Belt and the Kheis Belt. Further belts, which result from the collision of the Kalahari and Congo Cratons, are the Ghanzi-Chobe Belt and the Damara Belt in the northwestern part of the country. They were formed 1600 – 1000 Ma and 1000 – 541 Ma ago, respectively [Fadel et al., 2020].

The Passarge Basin in the central part of Botswana as well as the Nosop Basin in the west are overlain by younger sediments. In this study, the Limpopo Belt is of special interest since the Moijabana earthquake was located in its southwestern part (yellow star in Figure 4), close to the border of the Kaapvaal Craton. Other authors locate the earthquake in the Kaapvaal Craton [e. g. Gardonio et al., 2018] but nevertheless it lies near the junction of the Kaapvaal Craton and the Limpopo Belt. The Limpopo Belt can, based on lithologic and structural similarities, be divided into three zones: the Northern Marginal Zone, the Central Zone, and the Southern Marginal Zone [Ranganai et al., 2002]. The Moijabana event is located within the Southern Marginal Zone. Its epicenter is far from any seismic active area. The nearest seismically active region is the Okavango Rift Zone (ORZ) at > 300 km to the northwest. The ORZ is located in parts of the Damara and Ghanzi-Chobe Belts and belongs to a southwest branch of the EARS [Bufford et al., 2012].

2 The Botswana intraplate Earthquake on 3 April 2017

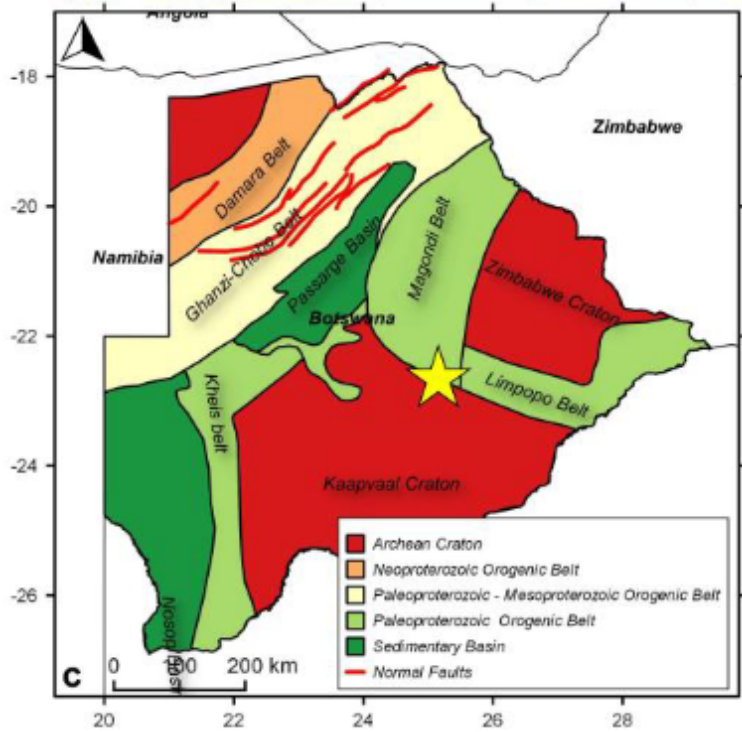


Figure 4: Tectonic map of Botswana. The map outlines Precambrian tectonic units in Botswana. The yellow star marks the location of the Mojabana earthquake. Red lines show the Okavango fault system. Source: Albano et al. [2017].

In summary, the old Archean cratons are tectonically stable regions and therefore, Botswana only shows a low level seismicity. This raises the question: What has or may have triggered the 2017 Botswana intraplate earthquake?

2.3 Trigger Hypothesis

There are several hypothesis on a trigger mechanism of the Mojabana earthquake. Albano et al. [2017] have investigated whether anthropogenic activities due to nearby gas extractions were the cause of the 3 April 2017 earthquake. Using Interferometric Synthetic Aperture Radar (InSAR) data, they estimated geometric and kinematic characteristics of a causative fault. The authors refute an anthropogenic origin. They observed an incompatibility between fault geometry and retrieved focal mechanism with the hypothetical stress perturbation. The latter is caused by gas extractions in the nearby area. Thus, the Mojabana earth-

2.3 Trigger Hypothesis

quake is classified as a natural intraplate event. Albano et al. eventually refer to the study from Kolawole et al. [2017], stating that extensional forces triggered the earthquake. Based on Differential Interferometric Synthetic Aperture Radar (DInSAR) analysis, aeromagnetic and gravity data, Kolawole et al. associate the Mojabana event with the extensional reactivation of Neoproterozoic thrust sheets within the Limpopo Belt.

However, [Gardonio et al. \[2018\]](#) explain the trigger mechanism of the Mojabana earthquake with fluids originating from the upper mantle. Because of the high temperatures in the lower crust at hypocentral depths, rocks should deform viscously instead of breaking. They state that a local pulse of fluids caused an embrittlement of the lower crust leading to failure. These fluids may have contributed to an elevation of the pore fluid pressure to sublithostatic level resulting in a decrease of the mechanical strength of the host rock and thus may have enabled rupture. The presence of significant amounts of fluids in the upper mantle beneath southern Africa supports this explanation. For instance, Kimberlite outcrops that form in carbonate-rich magma [Kamenetsky et al., 2014] can be found in southern Africa. They require H₂O- and CO₂-rich fluid phases from the mantle to realize the rapid melt ascent through the crust [Russell et al., 2012]. In the Okavango basin, a thermal anomaly hints at the existence of fluids in the mantle. The Okavango basin lies approximately 350 km northwest of the Mojabana epicenter (Figure 4). Leseane et al. [2015] interpret these irregularities as the signature of fluids advected from a metasomatised lithospheric mantle. Gardonio et al. [2018] mention that the two swarm-like foreshock sequences (see section 2.1) may be further evidence for upward fluid migration in a critically loaded fault network, eventually leading up to the larger main event.

The results from Moorkamp et al. [2019] from a magneto-telluric model cannot confirm the hypothesis put forward by Gardonio et al. [2018] as the magneto-telluric model does not show the expected features of a fluid mantle reservoir. However, they can neither refute the trigger hypothesis with fluids. Therefore, Moorkamp et al. suggest a weak zone in the upper mantle beneath the Mojabana epicenter. The authors interpret a low-velocity zone underneath the Mojabana event as region of reduced grain size, indicating a weak mantle and thus being responsible for the 3 April 2017 event.

2 The Botswana intraplate Earthquake on 3 April 2017

The authors [Materna et al. \[2019\]](#) propose a zone of weakness as source for the Mojabana earthquake likewise. They suggest that the Limpopo Belt, in which the event is located, is an ancient zone of weakness between the Archean Kaapvaal and Zimbabwe Cratons. Hence, the Mojabana earthquake may have occurred in response to stress accumulations in the EARS [Materna et al., 2019].

In contrast, [Fadel et al. \[2020\]](#) consider a different underlying cause. Whereas Gardonio et al. [2018] assessed fluids from the mantle, Fadel et al. connect the Mojabana earthquake to the EARS. They explain their approach that the normal faulting focal mechanism of the Mojabana event suggests a link to an extensional rifting system. The authors conclude that fluids or melt activated brittle failure, causing the crust to break. They inverted Rayleigh wave dispersion data obtained from ambient noise and teleseismic earthquakes in order to present a shear wave velocity model of Botswana. In their illustration, the low-velocity shear wave zone beneath the EARS acts as conduit for the fluids. These then trigger the local seismicity.

In 2020, [Chisenga et al. proposed a crustal thickness model of Botswana to tackle remaining discrepancies in the origin of the Mojabana earthquake. Besides this, existing crustal structure models \[e. g. Fadel et al., 2018; Kachingwe et al., 2015\]](#) do not provide sufficient resolution in the study area underneath the Mojabana earthquake. The authors analyzed gravity data to estimate the crustal setting of Botswana. Their model reveals a zone of thinned crust (~ 40 km thickness) in the vicinity of the Mojabana epicenter, surrounded by a relatively thicker crust (41–46 km) in cratonic regions and orogenic belts. A weak crust and mantle together with the local extensional stress regime result in crustal thinning in the otherwise thick cratonic setting [Moorkamp et al., 2019; Kolawole et al., 2017]. Chisenga et al. conclude that the thinned crust of the Mojabana event in combination with the local elevated heat flow and the local stress regime caused the Mojabana earthquake. In their view, thermal fluid movements from the mantle beneath the EARS caused the lower crust to erode and thin out. Thus, the region of the Southern Marginal Zone in the Limpopo Belt is classified as possible tectonic extension zone that could lead to further earthquakes [Chisenga et al., 2020].

3 Static Analysis of the Fault Plane

3.1 Methodical Approach of the static Analysis

The static analysis is a tool to describe the state of stress and static strength of the inferred fault plane for the Mojabana earthquake. Under the assumption of an Andersonian stress regime, meaning that one principal stress axis is vertical, we have to constrain the range of only four parameters to obtain a full description of the stress state and fault strength [Ulrich et al., 2019a]. Those parameters are the stress shape ratio ν , the fluid pressure ratio γ , the initial relative prestress ratio R_0 , and the direction of maximum horizontal compressive stress S_{Hmax} , all discussed below. Therefore, we aim to find the best configuration of these quantities that maximizes the relative prestress ratio R on our fault and thus favors an earthquake. The results are finally used in chapter 4 to verify whether our findings are suitable to host a large earthquake as it was observed.

First, in section 3.2 we analyze and combine different data sets (e. g. focal parameters, aftershock distribution of the Mojabana earthquake, and magneto-telluric data) to infer a possible fault plane for this event. In the next step (see section 3.3), we introduce the relative prestress ratio R and explain the input variables for the calculation of R on our fault. The results are discussed in section 3.4. They are compared to the outcome from Obermaier [2020], who obtained a different set of initial parameters that maximizes R on his differently oriented fault plane. We use the same data sets, Obermaier's findings are based on. Herein, we specify how different fault geometries – planar (this thesis) versus wavy [Obermaier, 2020] – affect the output of static analysis.

3 Static Analysis of the Fault Plane

3.2 Fault Geometry

To restrict both fault geometry and structure, different data sets are combined to a three-dimensional model in the visualization software Paraview. The model is shown in Figure 5. We depict the location of the hypocenter of the Mojabana earthquake (red dot) together with the distribution of aftershocks¹ (green dots). Additionally, we show a previously inferred fault plane (gray face) for this event. It dips at an angle of 73° to northeast. This wavy fault plane was ascertained by Obermaier [2020]. It was estimated from the surface expressions of the magneto-telluric model from Moorkamp et al. [2020]. Their model displays the conductivity distribution (or rather the resistivity distribution as the resistivity is the inverse of conductivity) in shallow depths. This fault plane is hereinafter referred to as *first* fault plane. As the Global Centroid Moment Tensor provides two solutions for the Mojabana earthquake, exactly two fault planes are able to fit the source parameters and explain the earthquake physics. In this thesis, we therefore consider a *second* fault plane solution.

Upon the magneto-telluric model (shown in Figure 6) as well as the locations of the main event and its aftershocks, we evaluate the new fault plane. Knowing that the underlying focal mechanism is normal faulting, we can cut down on the orientation of the second fault plane with respect to the first fault plane. The inferred second fault plane is almost perpendicular to the first one. We take abrupt changes in the conductivity model into account to determine the exact location. We tilt the plane so that it contains the hypocenter. Assuming a constant dip angle, we find that an angle of 28° fits the considerations best.

In order to model our inferred second fault plane, we transfer some coordinate points from the considerations in Paraview and join them together in Google Earth to a fault trace. Based on the fault line in cartesian coordinates (Universal Transverse Mercator), the fault plane is modeled to a depth of 33 km, assuming there the end of the seismogenic zone. We use the Python script *createFaultFromCurve.py*² to model the fault.

¹personal communication F. Kolawole, Oklahoma State University, Stillwater, Oklahoma, US, 2021

²<https://github.com/SeisSol/Meshing/tree/master/GocadRelatedScripts>, retrieved April 14, 2021; kindly provided by T. Ulrich, Ludwig-Maximilians-Universität, Munich, Germany

3.2 Fault Geometry

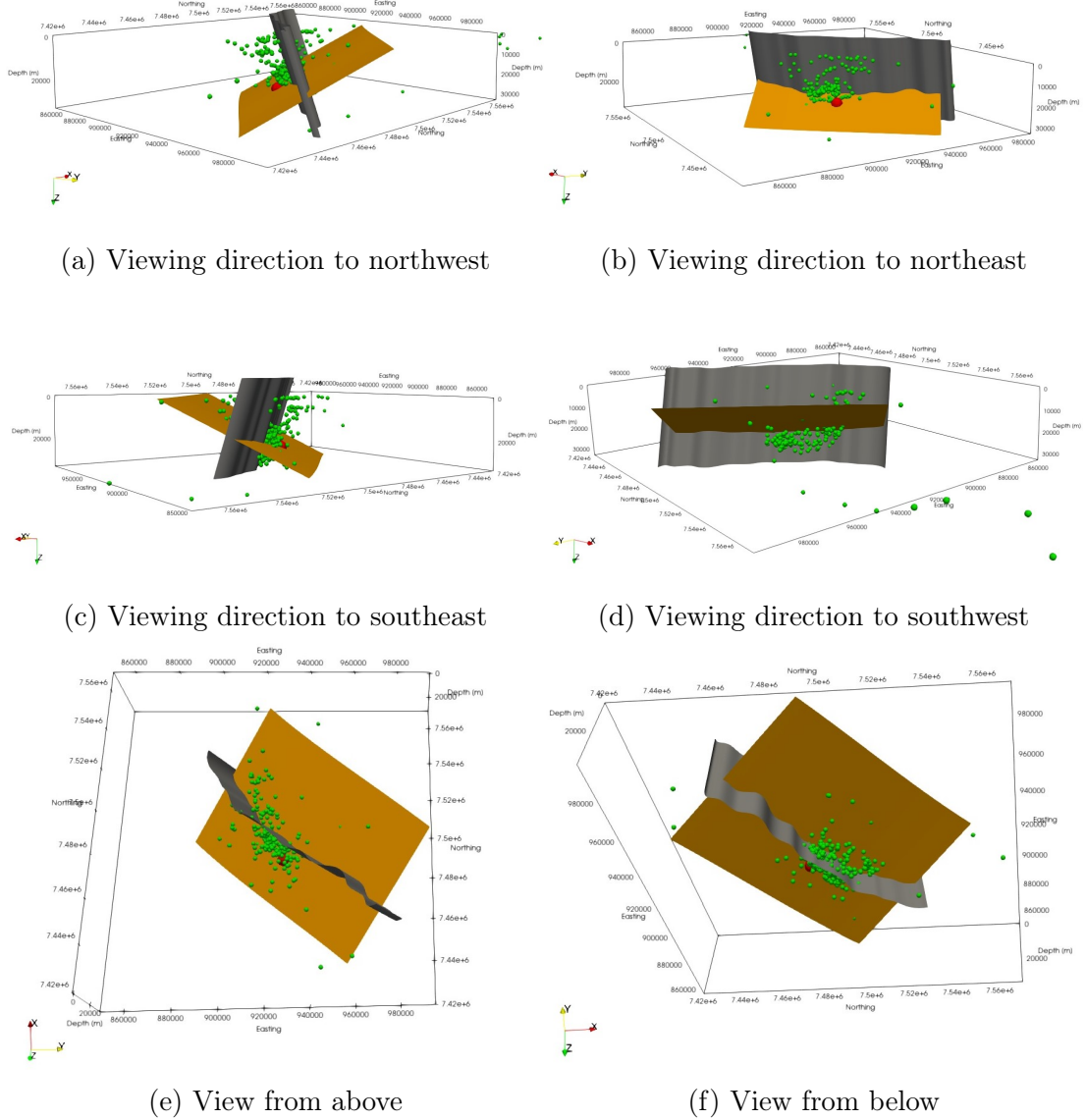


Figure 5: Visualization of both first and second fault plane. The three-dimensional model shows the location of the first fault plane (gray) and the second fault plane (orange). The red dot displays the hypocenter of the Moijabana earthquake. Green dots are aftershocks. Orientation of the axes: $x \equiv$ north (red), $y \equiv$ east (yellow), $z \equiv$ depth (green).

3 Static Analysis of the Fault Plane

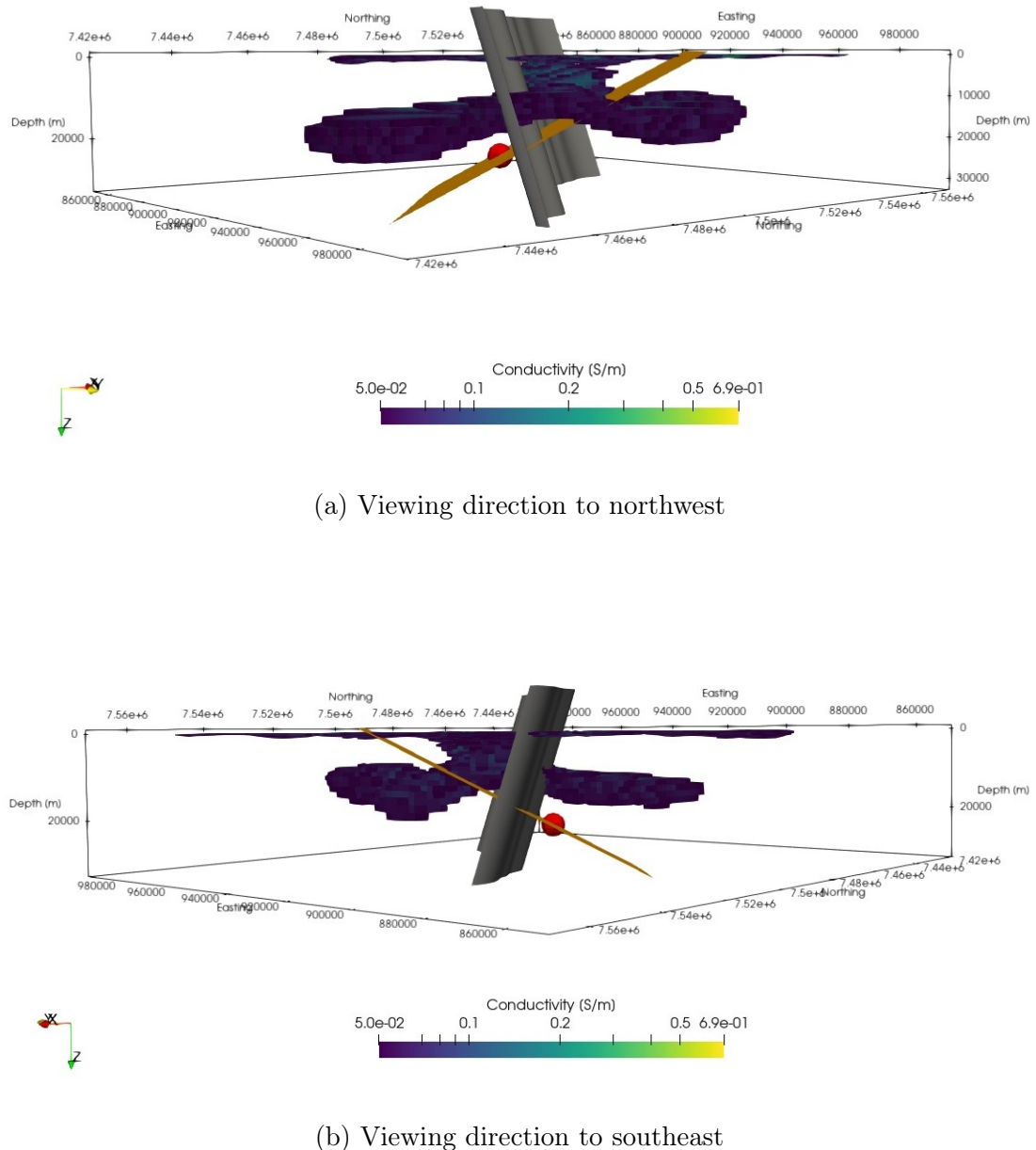


Figure 6: **Visualization of the conductivity.** The magneto-telluric model shows the conductivity in shallow depths in the vicinity of the earthquake (red dot). The lower threshold is at $0.05 \frac{\text{S}}{\text{m}}$. The gray face outlines the first fault plane. The second fault plane is depicted in orange. Orientation of the axes: $x \equiv$ north, $y \equiv$ east, $z \equiv$ depth.

3.2 Fault Geometry

Uncertainties in choosing the location of the second fault plane in Paraview and therefore in picking the fault trace in Google Earth remain since all considerations are based on geophysical models. Figure 7 displays two possible fault traces for the second fault plane against the background of the resistivity model at earth's surface. The orange trace represents the chosen one. The blue line depicts the possible further fault trace for the second fault plane. The gray line symbolizes the fault trace of the first fault plane. The resulting modeled fault plane corresponds to the orange face in Figure 5. We obtain a dip angle of 28° to southwest, striking northwest-southeast with 126° .

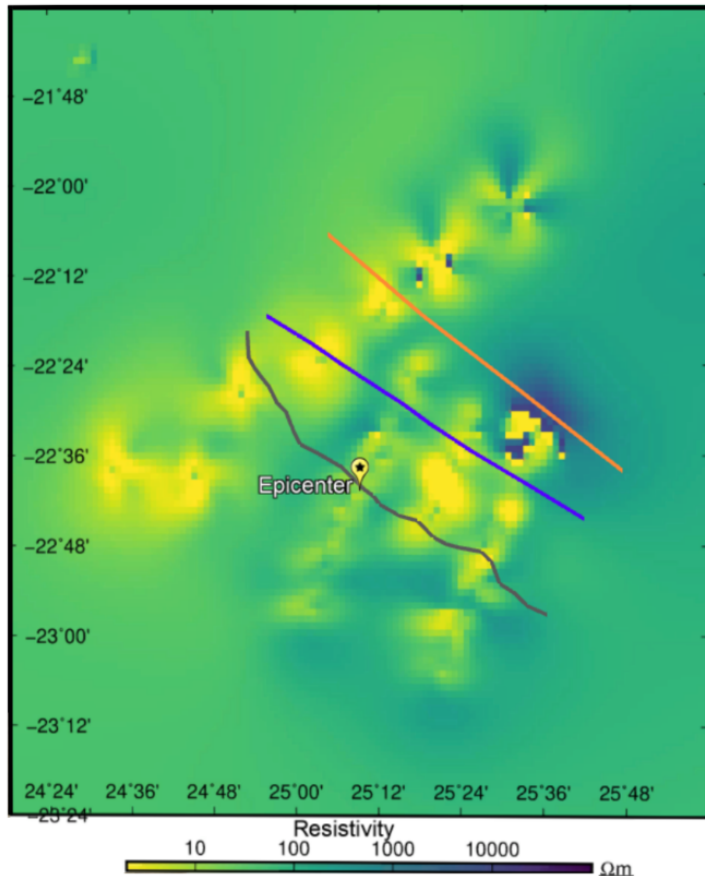


Figure 7: Location of the fault traces. The chosen fault trace (orange line) is shown with respect to the fault trace of the first fault plane (gray line) against the background of the resistivity at earth's surface. The blue line indicates a different fault trace for the second fault plane. The epicenter of the Mojabana earthquake is displayed. The coordinate axes are in degree longitude and degree latitude. North points to the top.

3 Static Analysis of the Fault Plane

3.3 Investigation of the Stress State

3.3.1 Relative Prestress Ratio and Parameters

The relative prestress ratio R is an important quantity to describe the spatially distributed strength of every point on the fault [Palgunadi et al., 2020]. The higher R , the weaker the fault is and the more likely it is to break. Failure is reached, meaning R is the highest, when the ratio of shear stress (τ) to effective normal stress (σ_n) is maximized, up to even being equal to the static frictional coefficient μ_s [Palgunadi et al., 2020]. Only a small portion of the fault reaching μ_s is sufficient to trigger dynamic rupture [Ulrich et al., 2019b]. The relative prestress ratio is calculated for every point on the fault as the ratio of potential stress drop $\Delta\tau$ to the breakdown strength drop $\Delta\tau_b$:

$$R = \frac{\Delta\tau}{\Delta\tau_b} = \frac{\tau_0 - \mu_d\sigma_n}{c + (\mu_s - \mu_d) \times \sigma_n} \quad (1)$$

It can also be expressed through initial shear traction τ_0 on the fault plane, static (μ_s) and dynamic (μ_d) friction coefficients, normal traction σ_n on the fault plane, and frictional cohesion c . Another value, the relative fault strength parameter S , can be derived from the relative prestress ratio as $S = \frac{1}{R} - 1$ [Palgunadi et al., 2020].

We need additional parameters to account for the frictional behaviour of the fault, its lithologic vicinity as well as the orientation of the stress axis, and the state of stress in general. The used values for these quantities are listed in Table 2. They are grouped in fixed and varied parameters. Most parameters are fixed, with exception of the stress shape ratio ν , the fluid pressure ratio γ , the initial relative prestress ratio R_0 , and the azimuth of maximum horizontal compressive stress S_{Hmax} . The four mentioned parameters are sufficient to fully characterize the stress state of the fault since we have an Andersonian stress regime [Ulrich et al., 2019a]. In the following subsections they are introduced and explained in detail.

The first fixed parameter is the static friction coefficient μ_s . Both μ_s and the dynamic friction coefficient μ_d are measured in laboratory experiments and they are constrained based on the Mohr-Coulomb theory of frictional failure. Here we

3.3 Investigation of the Stress State

set them to $\mu_s = 0.6$ and $\mu_d = 0.1$, following Ulrich et al. [2019b]. The frictional cohesion c is set to a small value ($c = 0.1$) to account for the closeness of our fault to earth's surface [Palgunadi et al., 2020].

The lithologic vicinity of our fault is characterized by a crustal density of $\rho = 2670 \frac{\text{kg}}{\text{m}^3}$ [Ramotoroko et al., 2016]. Together with the varied fluid pressure ratio γ , they are combined to the effective density ρ' , as described in subsection 3.3.3. For the computation of the stress tensor, we need to define a reference depth. Equal to the hypocentral depth of the Mojabana event, we set it to $z_{ref} = 23.5$ km, since we assume the fault to first break in this depth. It has to be noted that changing this quantity does not affect static analysis results much.

Assuming an Andersonian stress regime, we have to determine a principal stress axis which needs to be vertical. In our extensional case, the σ_1 -axis is vertical with $\sigma_1 > \sigma_2 > \sigma_3 > 0$. Therefore, S_V is set to 1. In order to run dynamic rupture simulations (to be discussed in chapter 4), the software SeisSol requires a coordinate vector with components $v_x = 0.1$, $v_y = 0.1$, and $v_z = 1$ [Obermaier, 2020].

Table 2: Applied parameters for the calculation of R . The table lists all parameters and their values that are required for the calculation of the relative prestress ratio on the fault.

Description	Parameter	Value	Variation
Initial relative prestress ratio	R_0	0.3	$0.2 \leq R_0 \leq 1.0$
Static friction coefficient	μ_s	0.6	
Dynamic friction coefficient	μ_d	0.1	
Frictional cohesion	c	0.1	
Crustal density	ρ	$2670 \frac{\text{kg}}{\text{m}^3}$	
Fluid pressure ratio	γ	0.95	$0.37 < \gamma < 1$
Effective density	ρ'	$134 \frac{\text{kg}}{\text{m}^3}$	$< 1682 \frac{\text{kg}}{\text{m}^3}$
Reference depth	z_{ref}	23.5 km	
Azimuth of maximum horizontal compressive stress	S_{Hmax}	142°	±40°
Vertical principal stress axis	S_V	1	
Stress shape ratio	ν	0.5	
Vector component x	v_x	0.1	
Vector component y	v_y	0.1	
Vector component z	v_z	1	

3 Static Analysis of the Fault Plane

After writing the discussed parameters in an initialization file, the Python script *displayUnstructuredVtk.py*³ is executed. It includes the input variables and accounts for an Andersonian setting. The script uses a series of further scripts, among them *computeR.py*³, which effectively calculates the relative prestress ratio R for every point on the fault. The output is discussed in section 3.4.

It should be noted that the R -ratio was plotted on the inferred fault from section 3.2 but its fault orientation was transposed into a new coordinate system. This is because the dynamic rupture simulation setup in chapter 4 requires another orientation of the coordinate axes. Thus, the x-axis points towards east, the y-axis points towards north, and the z-axis is oriented in height above earth's surface (negative depth), respectively.

3.3.2 The Stress Shape Ratio

The stress shape ratio ν relates the principal stress amplitudes to each other. According to Palgunadi et al. [2020] it is defined as:

$$\nu = \frac{\sigma_2 - \sigma_3}{\sigma_1 - \sigma_3} \quad (2)$$

The parameters σ_i with $i = \{1, 2, 3\}$ are the amplitudes of the principal stress axes. For our case, where σ_1 is vertical, a value of $\nu = 0.5$ means that the faulting regime is pure extension. $\nu < 0.5$ describes transpression, whereas $\nu > 0.5$, indicates transtension [Ulrich et al., 2019a]. Its value can be constrained from observations. For our application, the stress shape ratio is set to a constant value of $\nu = 0.5$, as the observed Mojabana earthquake shows an extensional regime with pure normal faulting.

3.3.3 The Fluid Pressure Ratio

The fluid pressure ratio γ is another parameter describing the static strength of the fault. In crustal regimes we assume that the pore fluid pressure P_f is

³<https://gitlab.lrz.de/thomas.ulrich/TuSeisSolScripts/-/tree/master/displayh5vtk>, retrieved April 14, 2021; kindly provided by T. Ulrich, Ludwig-Maximilians-Universität, Munich, Germany

3.3 Investigation of the Stress State

proportional to the lithostatic confining stress $\sigma_c(z) = \rho g z$ [Ulrich et al., 2019b]. These quantities are linked by the fluid pressure ratio as:

$$P_f = \gamma \sigma_c(z) = \gamma \rho g z \quad (3)$$

The parameter ρ or rather $\rho(z)$ is the (depth-dependent) density, g represents the gravitational acceleration ($g = 9.81 \frac{\text{m}}{\text{s}^2}$), and z denotes the depth [Palgunadi et al., 2020]. A hydrostatic state of stress is specified by $\gamma = 0.37$. If $\gamma > 0.37$, an overpressured state of stress is implied [Ulrich et al., 2019b].

The lithostatic confining stress is thus reduced by the pore fluid pressure to the effective confining stress $\sigma_{c'}(z)$ as:

$$\sigma_{c'}(z) = (1 - \gamma)\sigma_c(z) = \sigma_c(z) - \gamma\sigma_c(z) \stackrel{(3)}{=} \sigma_c(z) - P_f \quad (4)$$

For the calculation of the R -ratio on our fault, the fluid pressure ratio is included in the effective density ρ' with $\rho' = \sigma_{c'}(z)/gz$:

$$\rho' = (1 - \gamma)\rho \quad (5)$$

According to Ramotoroko et al. [2016], we assume the average crustal density in the vicinity of the Moijabana earthquake to be $\rho = 2670 \frac{\text{kg}}{\text{m}^3}$ (Table 2). The resulting effective density varies with increasing fluid pressure ratios as shown in Table 3.

Table 3: Variation of ρ' . The effective density ρ' is indirectly proportional to the fluid pressure ratio γ . The values are computed after Equation 5 for $\rho = 2670 \frac{\text{kg}}{\text{m}^3}$. The table lists rounded values for ρ' .

γ	$\rho' [\frac{\text{kg}}{\text{m}^3}]$
0.37	1682
0.45	1469
0.55	1202
0.65	935
0.75	668
0.85	401
0.95	134

3 Static Analysis of the Fault Plane

It has to be noted that the fluid pressure ratio has a great influence on the stress drop. After Ulrich et al. [2019a], an estimation of the dimension of the stress drop can be expressed as:

$$d\tau \sim R_0(\mu_s - \mu_d)(1 - \gamma)\sigma_c \stackrel{(4)}{=} R_0(\mu_s - \mu_d)\sigma_c' \quad (6)$$

The average stress drop is thus limited by an elevated pore fluid pressure [Palgunadi et al., 2020], under the assumption of a constant initial relative prestress ratio R_0 (introduced hereinafter). μ_s as well as μ_d are the static and dynamic friction coefficients, respectively (Table 2). $d\tau$ is therefore a fundamental value controlling the size of an earthquake, the average slip on the fault, and the rupture velocity. For our application, we need an overpressured stress state to obtain a realistic amount of slip in the dynamic rupture simulation⁴. Therefore, we set $\gamma > 0.37$, although we do not yet know the role that fluids play in the case of the Moijabana earthquake.

3.3.4 The initial relative Prestress Ratio

The next parameter that governs the state of stress is the initial relative prestress ratio R_0 . It describes how close a virtual, optimally oriented fault is to failure. This failure criterion is determined by the Mohr-Coulomb theory [Aochi & Madariaga, 2003]. The initial relative prestress ratio indicates the initial relative strength of a fault in its optimal orientation [Palgunadi et al., 2020]. Under homogeneous stress conditions, an optimally oriented fault would reach failure before any differently oriented fault [Ulrich et al., 2019b]. At this point the ratio of shear to normal stress is maximized and equals μ_s (see subsection 3.3.1).

A value of $R_0 = 1$ states a critical loading stress on an optimally oriented fault, meaning that the Coulomb stress is maximized [Ulrich et al., 2019a]. Usually, this threshold is not reached since the fault is not necessarily optimally oriented. Therefore, the relative prestress ratio is less or equal to the initial relative prestress ratio ($R \leq R_0$). Equation 6 on page 22 shows the contribution of R_0 to the average stress drop. It is evident that the initial relative prestress ratio has a large influence on the stress drop and thus decisively controls the rupture process.

⁴personal communication T. Ulrich, Ludwig-Maximilians-Universität, Munich, Germany, 2021

3.3 Investigation of the Stress State

As the parameter space of R_0 is fully unknown, we start with a low R_0 . We then calculate the relative prestress ratio R on our fault, whilst varying the parameter S_{Hmax} (see subsection 3.3.5). We eventually increase R_0 in steps of 0.1, until the threshold of $R_0 = 1$ is reached. The best configuration that maximizes R on our fault is discussed in section 3.4.

3.3.5 The Azimuth of maximum horizontal compressive Stress

Since the stress regime is characterized by an Andersonian setting, the direction of the azimuth of maximum compressive horizontal stress S_{Hmax} is the final parameter that is necessary to describe the state of stress on our fault. In the Andersonian case, it coincides with the horizontal projection of the largest subhorizontal stress [Ulrich et al., 2019b]. As we have a normal faulting mechanism (σ_1 being vertical), S_{Hmax} is oriented along the principal stress axis σ_2 .

Observed values for S_{Hmax} can be extracted from the World Stress Map [Heidbach et al., 2016b] and are linked to tectonic processes. Table 4 lists values of S_{Hmax} for the vicinity of the Mojabana earthquake. They are however not well constrained, as their quality factors are bad (E quality).

Table 4: Values of S_{Hmax} from the World Stress Map. The listed values indicate the directions of S_{Hmax} in the nearest vicinity of the Mojabana earthquake. They are extracted from the World Stress Map [Heidbach et al., 2016b]. The quality factor is bad (E).

WSM-ID	Latitude [°]	Longitude [°]	Azimuth [°]	Quality
wsm03860	-24.5 S	27.0 E	138	E
wsm04573	-25.0 S	24.0 E	142	E
wsm04574	-22.5 S	23.5 E	143	E
wsm04575	-21.5 S	27.5 E	22	E

Due to large uncertainties in the parameter space of S_{Hmax} , we vary this value between +6

102°–182° in steps of 10° to constrain its range. We therefore expect a significant influence of S_{Hmax} on the calculation of the relative prestress ratio on our fault.

3 Static Analysis of the Fault Plane

3.4 Results and Discussion

3.4.1 Constrained Parameters

Instead of plotting the absolute value of R on the fault, we plot R relative to R_0 as the normalized relative prestress ratio $\frac{R}{R_0}$. With this normalization it is easier to compare the results for varying values of the initial relative prestress ratio. In the figures below, the distribution of the $\frac{R}{R_0}$ -ratio is represented by the coloration on the fault. The redder the color, the higher is the normalized relative prestress ratio. We choose the configuration for which $\frac{R}{R_0}$ is the largest, meaning R is the closest to R_0 . The parameter range is down-scaled for each calculation since a ratio of $\frac{R}{R_0} = 1$ is hardly reached for our configurations. The closer the quotient is to this threshold, the weaker the fault and the sooner it will fail and rupture into an earthquake.

To begin with, we increase R_0 from 0.2 to 1.0 in steps of 0.1, whilst setting the stress shape ratio constant at $\nu = 0.5$ and the fluid pressure ratio to lithostatic conditions at $\gamma = 0.95$. For each configuration, S_{Hmax} is varied between 102° – 182° . Figure 8 shows the resulting plots of the normalized R -ratio for every point on the fault. Note that the color bar ranges from 0.100 to 0.600. As we want to maximize R relative to R_0 on our fault, it is obvious to choose the configuration depicted in Figure 8b, where R_0 is set to 0.3.

In the second step, the parameter space of S_{Hmax} is constrained. As expected, S_{Hmax} strongly influences static analysis results, since this value is subject to large uncertainties. We vary S_{Hmax} in steps of 10° starting from 102° , up to 182° . Figure 9 displays the normalized distribution of R on our fault with the chosen value of $R_0 = 0.3$. Values between 122° – 142° are most suitable. These findings match roughly with most observations of the World Stress Map (Table 4). A closer look reveals an angle of 134° for the direction of maximum horizontal compressive stress that maintains the highest normalized R -ratio. Therefore, this value is chosen for the dynamic rupture simulation. However, it should be noted that all values in the range of 130° – 139° are well comparable and that deviations first occur in the third decimal. Nonetheless, no configuration shows critical loading ($R \approx R_0$) of the fault. Thus, we do not expect rupture to nucleate on this fault.

3.4 Results and Discussion

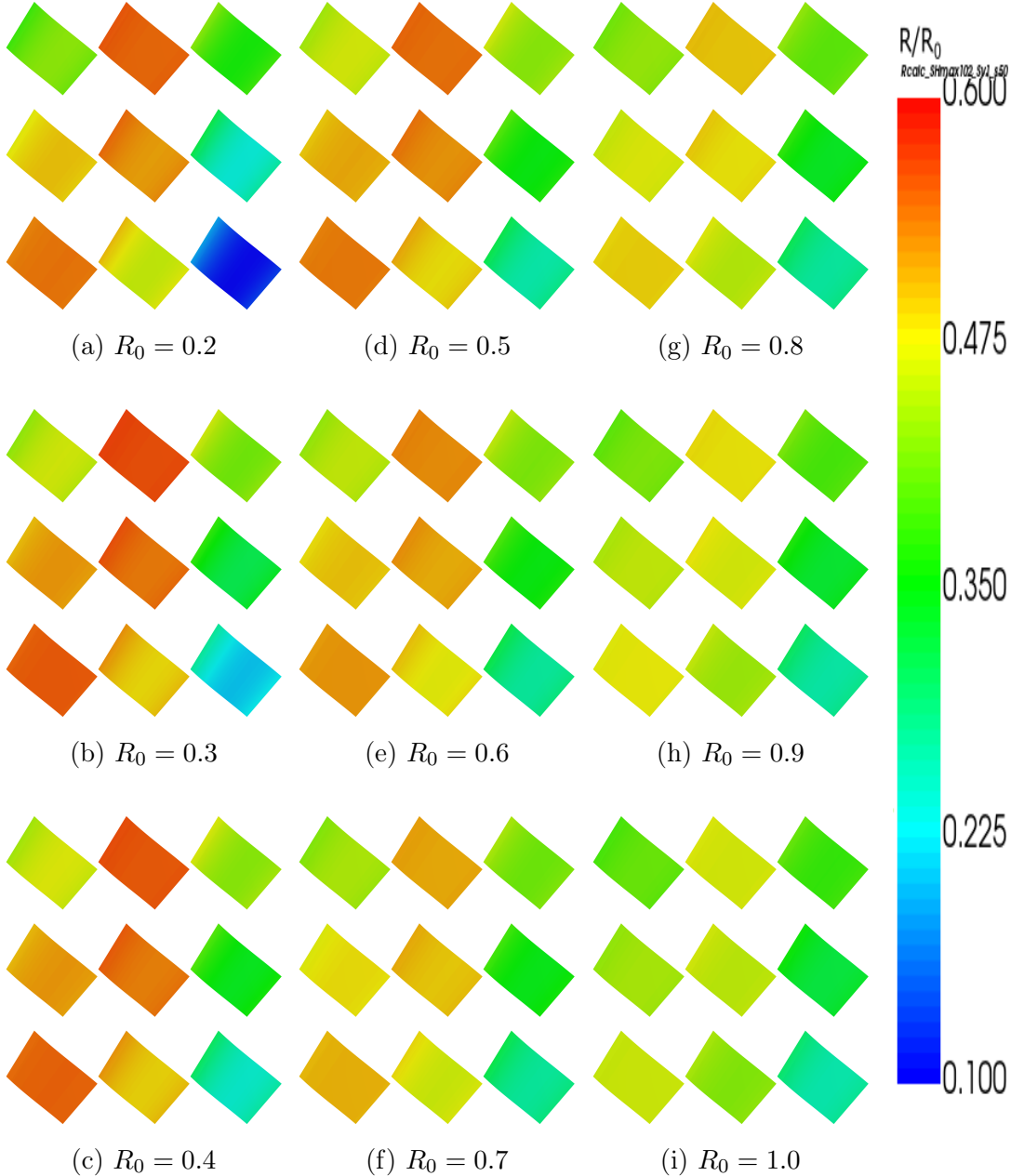


Figure 8: Normalized distribution of R under variation of R_0 . The plots show the calculated $\frac{R}{R_0}$ -ratio on the fault under the variation of R_0 from 0.2 to 1.0. Within each plot, S_{Hmax} is varied from 102° to 182° . The fluid pressure ratio is set to lithostatic conditions ($\gamma = 0.95$).

3 Static Analysis of the Fault Plane

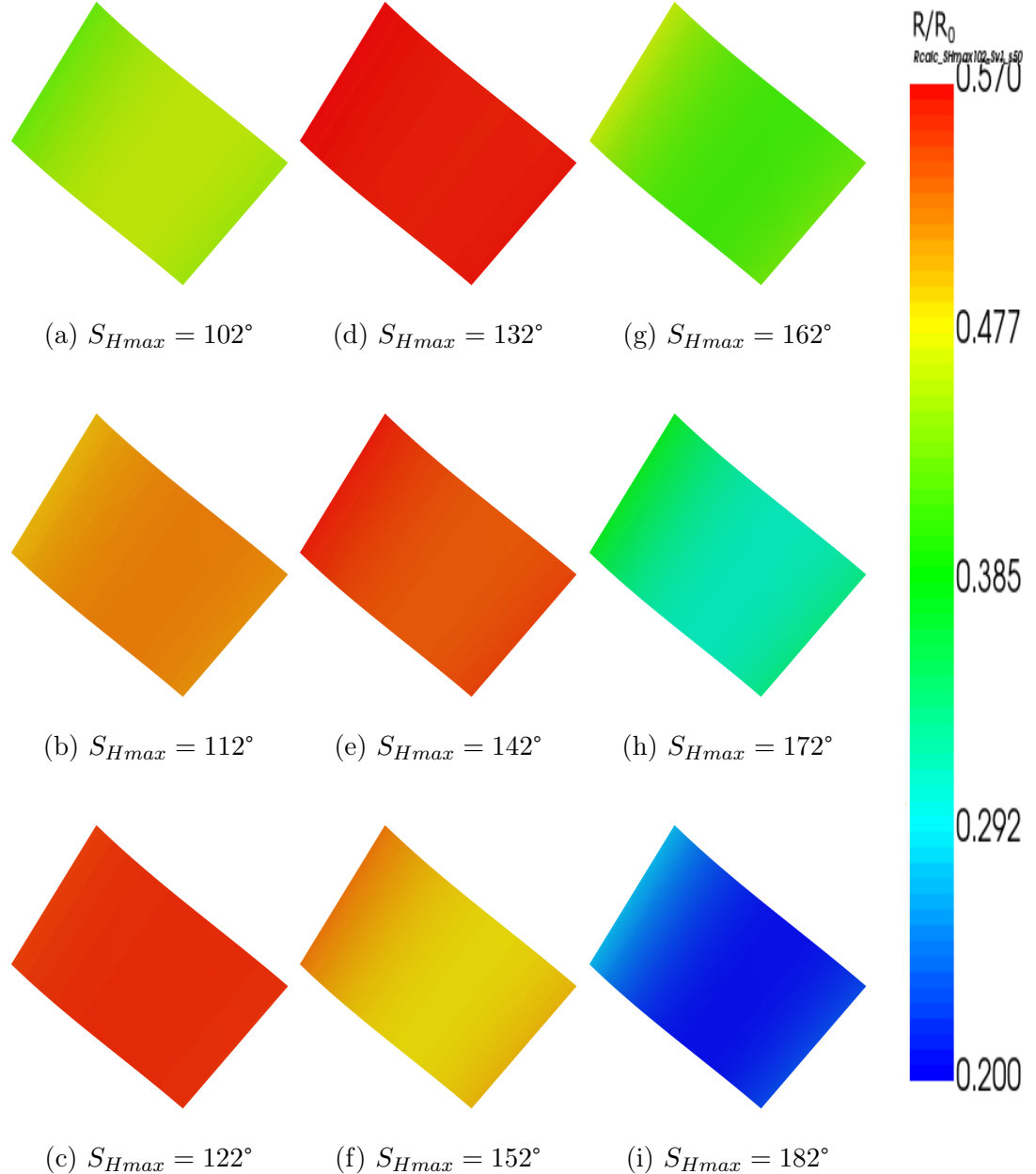


Figure 9: Normalized distribution of R under variation of S_{Hmax} for $R_0 = 0.3$. A closer look in Figure 8b shows the $\frac{R}{R_0}$ -ratio on the fault under the variation of S_{Hmax} from 102° to 182° . R_0 is constant at 0.3. The fluid pressure ratio γ is set to 0.95.

3.4 Results and Discussion

Interestingly, the variation of the fluid pressure ratio after Table 3 does not influence static analysis results. This is remarkable, as this quantity plays an important role in controlling the average stress drop (see Equation 6). During the calculations, the fluid pressure ratio is constantly set to lithostatic conditions ($\gamma > 0.37$). To pursue the investigation of the trigger mechanism of the Mojabana earthquake, fluids in the region of the hypocenter should be decisively taken into account. There are former studies (e. g. Chisenga et al. [2020], Fadel et al. [2020], see section 2.3) that suspect a connection between fluids from the East African Rift System and the source of the 2017 Botswana earthquake. Consequently, the variation of the fluid pressure ratio in the dynamic rupture simulations and the evaluation of its outcome are mandatory.

As previously mentioned in subsection 3.3.2, the stress shape ratio is held constant at $\nu = 0.5$ during static analysis. As there are no contradictions regarding the focal mechanism of the Mojabana event – all authors agree on an extensional normal faulting mechanism – there is no need to constrain the parameter space of this quantity.

3.4.2 Evaluation of different Fault Geometries

In this subsection, we want to quantify how different fault geometries affect the fault's state of stress and static strength. In order to do so, we compare the outcome of static analysis on the wavy *first* fault plane (gray face in Figure 5) from Obermaier [2020] with our planar fault geometry of the *second* fault plane (orange face in Figure 5). Obermaier selected $R_0 = 0.7$, $S_{Hmax} = 132^\circ$, $\gamma = 0.95$, and $\nu = 0.5$ as best configuration to maximize the R -ratio on his fault.

Similar to subsection 3.4.1, we plot the normalized relative prestress ratio $\frac{R}{R_0}$ on both the wavy and the planar fault, to better compare the results. Figure 10 shows the distribution of the normalized relative prestress ratio along the first fault plane. The color scale and thus $\frac{R}{R_0}$ reach a value of 0.800. Figure 10d (together with Figure 10e) was identified as most suitable since the highest values for the normalized relative prestress ratio are reached. Therefore, Obermaier [2020] chose $S_{Hmax} = 132^\circ$ as initial parameter for the dynamic rupture simulation.

3 Static Analysis of the Fault Plane

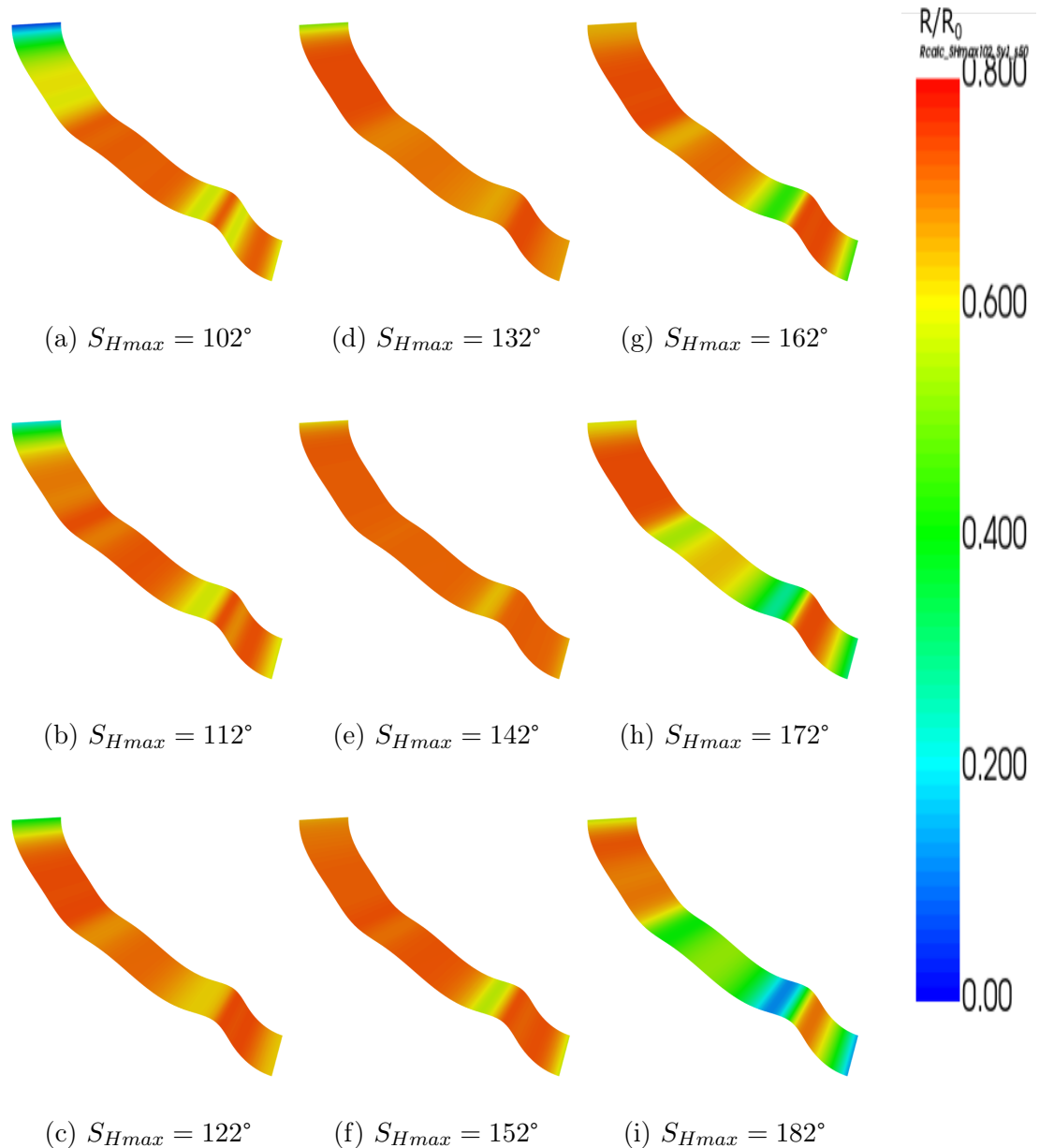


Figure 10: Normalized distribution of R on the first fault plane under variation of S_{Hmax} . The plots show the calculated $\frac{R}{R_0}$ -ratio on the wavy first fault plane under the variation of S_{Hmax} from 102° to 182° . R_0 is constant at 0.7. The fluid pressure ratio γ is set to 0.95.

3.4 Results and Discussion

The above-mentioned values are subsequently plotted on the second fault plane. Results for the distribution of the normalized relative prestress ratio are shown in Figure 11. It should be noted that the color range was down-scaled to 0.260–0.520 as higher values of $\frac{R}{R_0}$ are not reached. The visualization of the normalized relative prestress ratio on the second fault plane confirms Obermaier’s observations. For $R_0 = 0.7$, we find likewise that on our fault plane the highest $\frac{R}{R_0}$ -ratios are obtained with $S_{Hmax} = 132^\circ$.

In direct comparison of Figure 10 and Figure 11 it is obvious that in the surroundings of smoothed kinks the normalized relative prestress ratio changes almost abruptly. This indicates that the fault’s texture has a major influence on static analysis and that small spatial variations in the fault geometry may lead to huge differences in the outcome. Nonetheless, no setup – neither the planar geometry nor the wavy one – leads to a critical loading of the fault, meaning $R \approx R_0$.

Considering the two possible geometries, the first fault plane is better suited to host a large earthquake as it was observed since all configurations sustain significantly higher normalized R -ratios. To reinforce this conclusion, our planar fault plane exhibits a higher fault strength as the normalized relative prestress ratio is comparably low. Therefore, a small change in stress would probably not trigger an earthquake on the second fault plane as it could be the case in the first fault plane. Consequently, performing dynamic rupture on the second fault plane and comparing its output with the simulation results from Obermaier [2020] may validate the proper fault geometry of the Moijabana earthquake.

3 Static Analysis of the Fault Plane

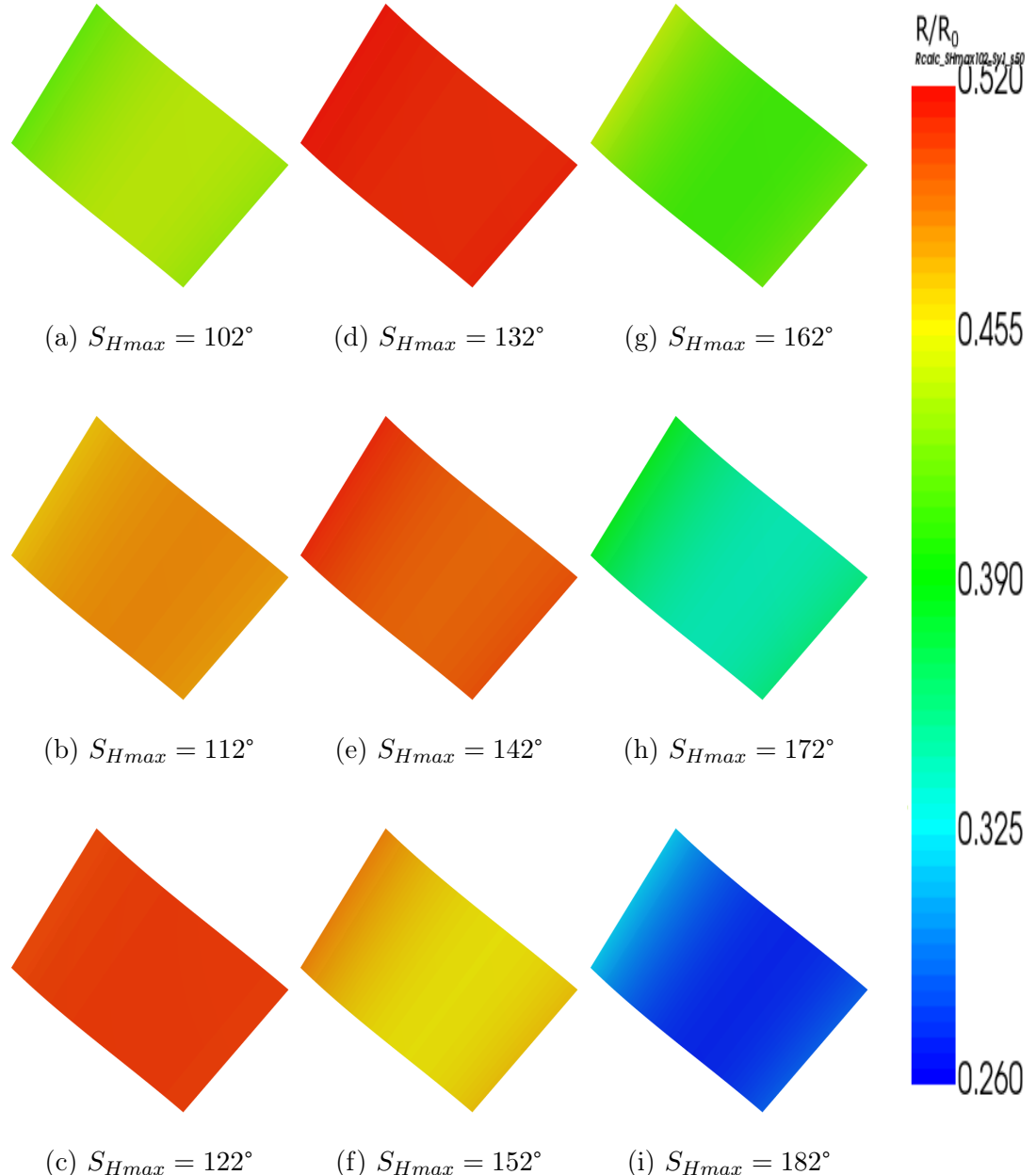


Figure 11: Normalized distribution of R on the second fault plane under variation of S_{Hmax} . The plots show the calculated $\frac{R}{R_0}$ -ratio on the planar second fault plane under the variation of S_{Hmax} from 102° to 182° . R_0 is constant at 0.7. The fluid pressure ratio γ is set to 0.95.

4 Simulation of the Rupture Dynamics

4.1 Methodical Approach of the dynamic Rupture

To run dynamic rupture simulations, we use the open-source software SeisSol⁵. The software simulates the complete three-dimensional seismic wavefield and its propagation in realistic media with complex geometry. It uses tetrahedral meshes and accounts for different material properties (e. g. elastic, viscoelastic, viscoplastic) to approximate geological features [Gabriel et al., 2021]. SeisSol is based on the so-called Arbitrary high-order accurate DERivative Discontinuous Galerkin method and solves the wave equation numerically on every point on the fault for all time steps. The code is freely available⁶.

The goal of the dynamic rupture simulation is to determine the earthquake nucleation process and its propagation along the fault for given stresses and frictional conditions. Dynamic rupture resolves how and where the rupture eventually stops and how the slip propagates along the fault plane.

Input variables are the fault geometry, frictional strength of the fault, initial and regional stress conditions, and lithological properties [Palgunadi et al., 2020]. These values are submitted in input files, discussed in subsection 4.2.2. Besides this, the simulation setup requires a mesh which discretizes the geometry around the fault (see subsection 4.2.1). After running the simulation on the supercomputer SuperMUC in Garching near Munich, the output can be visualized in Paraview (see section 4.3).

⁵<https://www.seissol.org/>; retrieved April 28, 2021

⁶<https://github.com/SeisSol/SeisSol>; retrieved April 28, 2021

4 Simulation of the Rupture Dynamics

4.2 Dynamic Rupture modeling Setup

4.2.1 Mesh Generation

We use the meshing software Simmodeler⁷ to discretize the geometry around the fault. The model dimensions are defined with a box of the size of 255 km × 253 km × 118 km, analog to Obermaier [2020]. These values are sufficient to avoid reflexions of the fastest P waves at the edges of our model, assuming a maximum simulation period of 30 s and a P wave velocity of $v_P = 8.75 \frac{\text{km}}{\text{s}}$ [Obermaier, 2020].

The calculation of the maximum traveled distance results in 262.5 km. Although being slightly larger than our model domain, this discrepancy may not be decisive. Nevertheless, it should be kept in mind in case of appearing reflexions. There is no need to account for topography, as our fault does not intersect the surface.

We set the size of the elements close to the fault at 300 m, increasing to 10 km on the regional domain. The gradation rate is set to 0.3 for the model so that the mesh coarsens away from the fault. We aim to get a good quality for the mesh. Therefore, we set the aspect ratio of the surface shape metric to 6.0 and the volume shape metric at 12.0; the smaller this value, the better. The software tries to enforce these values.

The resulting mesh consists of 3 338 830 tetrahedral elements. The mesh statistics reveal the highest aspect ratio of 14.1. Aspect ratios for simple meshes are < 10, whereas the aspect ratio for complex meshes can reach up to 40 [The SeisSol Team Revision, 2021]. In our mesh, 99 % of the elements have aspect ratios smaller than 10, only 7430 elements show aspect ratios greater than 10. No element is exceeding an aspect ratio of 20. The generated mesh is shown in Figure 12. It is stored in a mesh file needed below.

4.2.2 Input Files

The input files include initial stress conditions for the Andersonian setting, material properties such as density and Lamé parameters, the nucleation stress conditions, and our findings from static analysis. These model parameters are stored in YAML ("YAML Ain't Markup Language") files.

⁷<https://seissol.readthedocs.io/en/latest/meshing-with-simmodeler.html>; retrieved April 28, 2021

4.2 Dynamic Rupture modeling Setup

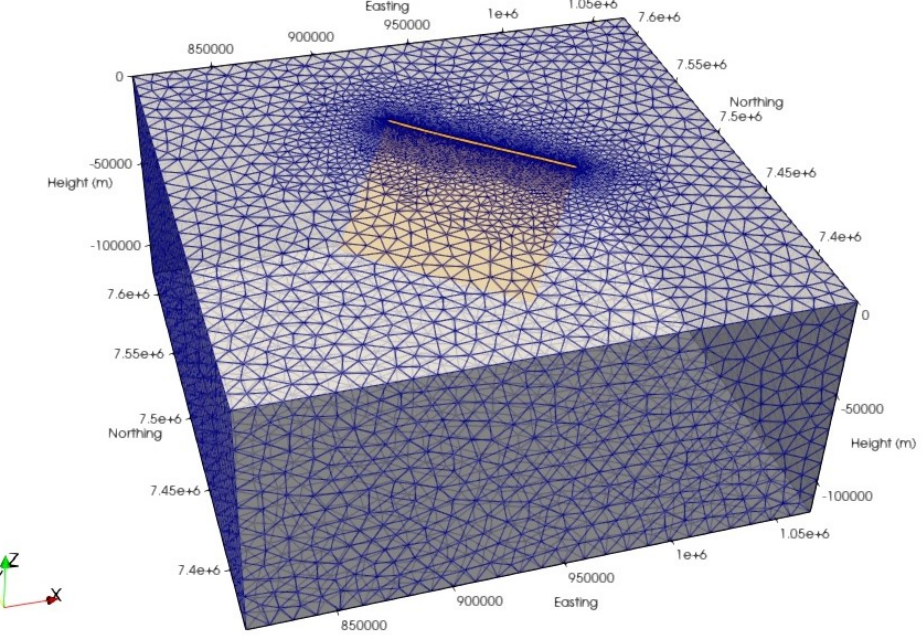


Figure 12: Visualization of the generated mesh. The mesh discretizes the model domain. It is coarsened away from the fault. Orientation of the axes: $x \equiv$ east, $y \equiv$ north, $z \equiv$ height.

Additionally, a parameter file is needed. The parameter file consecutively reads the YAML material file, the YAML model file, and loads the mesh file containing the model resolution. The YAML model file itself reads both the YAML initial stress and the YAML nucleation stress files. The parameter file specifies among others friction law parameters. In our case, we account for strong velocity weakening. The rapid weakening friction law parameters are adopted from Palgunadi et al. [2020]. They are listed in Table 5. The underlying equations for the parameters listed hereinafter are introduced in Ulrich et al. [2019b]. The direct effect parameter a and the weakening slip velocity V_W are depth-dependent as $0.01 \cdot z$ and $0.1 \cdot z$, respectively. The evolution effect parameter is set to $b = 0.014$. At a reference slip velocity of $V_0 = 10^{-6} \frac{\text{m}}{\text{s}}$, the steady-state friction coefficient f_0 is equal to μ_s as 0.6 (see subsection 3.3.1). The steady-evolution distance L has a value of 0.2 m. Following Ulrich et al. [2019b], we assume strong dynamic weakening ($f_w = 0.1$), thus f_w being equal to the dynamic friction coefficient μ_d from static analysis (see subsection 3.3.1). The initial slip rate is set to $V_{ini} = 10^{-16} \frac{\text{m}}{\text{s}}$.

4 Simulation of the Rupture Dynamics

Table 5: Dynamic rupture friction parameters. The required friction parameters for the dynamic rupture setup are adopted from Palgunadi et al. [2020]. The variable z denotes the depth in meter.

Description	Parameter	Value
Direct effect parameter	a	$0.01 \cdot z$
Evolution effect parameter	b	0.014
Reference slip velocity	V_0	$10^{-6} \frac{\text{m}}{\text{s}}$
Steady-state friction coefficient at V_0	f_0	0.6
Steady-evolution distance	L	0.2 m
Weakening slip velocity	V_W	$0.1 \cdot z$
Fully weakened friction coefficient	f_W	0.1
Initial slip rate	V_{ini}	$10^{-16} \frac{\text{m}}{\text{s}}$

4.3 Results and Discussion

4.3.1 First Simulation

We run the first simulation on SuperMUC with the constrained initial parameters $\nu = 0.5$, $\gamma = 0.95$, $R_0 = 0.3$, and $S_{Hmax} = 134^\circ$ (see subsection 3.4.1). After a period of 1.3 s the simulation is aborted. Because of a too low moment rate ($M_W < 0$) rupture does not nucleate. Consequently, no slip on the fault is observed.

We explain these findings as our R_0 is very small, implicating a statically strong fault. It is certain that a significantly higher R_0 is necessary to bring the fault to failure. Nonetheless, theoretically it should also break with a low R_0 . The inferred second fault plane is thus far from optimally oriented in the meaning of the Mohr-Coulomb theory of failure (see subsection 3.3.4).

We conclude that our inferred fault plane is unsuitable to host a large M_W 6.5 earthquake as it was observed. These considerations confirm the strong effect of the fault geometry on the rupture process as previously stated by Palgunadi et al. [2020]. Additionally, the results validate the presumption from static analysis (see subsection 3.4.1), expecting that rupture may not nucleate on this fault. No indications regarding the trigger mechanism of the Mojabana earthquake can be made with these findings.

4.3.2 Second Simulation

General Findings

The second simulation runs with the input parameters $\nu = 0.5$, $\gamma = 0.95$, $R_0 = 0.7$, and $S_{Hmax} = 132^\circ$ (see subsection 3.4.2). Similar to the first simulation, the nucleation stress is much too low and rupture does not nucleate. To reach failure, we increase the relative prestress ratio in the nucleating area to $R = 30$. This value is rather high and unconventional for earthquakes but it causes the rupture to nucleate. Additionally, the effective confining stress is changed to $\sigma_{zz} = -2670 \frac{\text{kg}}{\text{m}^3} \cdot 9.81 \frac{\text{m}}{\text{s}^2} \cdot 23\,500 \text{ m}$. This value for σ_{zz} is inconsistent with the used fluid pressure ratio in the YAML initial stress file but it nonetheless drives nucleation. It confirms the large influence of the fluid pressure ratio on the size of the generated earthquake as stated in Equation 6.

Comparing our findings with previous results [see Kolawole et al., 2017; Albano et al., 2017; Gardonio et al., 2018; Materna et al., 2019; Obermaier, 2020] is not meaningful as our model parameters are rather artificial and would not correspond to nature. These observations confirm that the inferred fault plane is not appropriate to generate an earthquake as large as it was recorded. In consequence, we are not able to discuss the influence of the fluid pressure ratio properly.

Fault Output

To start with, SeisSol simulates fault outputs such as slip distances in strike and dip directions, accumulated slip or the slip rates. In our model the accumulated slip on the fault reaches 3.7 m in the direct vicinity of the hypocenter. Figure 13 displays the dimensions of the rupture. After a period of 2.3 s rupture stops. The background stress is probably not sufficient to further propagate the rupture. The slip rates in the closest surroundings of the nucleating area are about $17 \frac{\text{m}}{\text{s}}$. The ruptured area measured approximately $10 \text{ km} \times 10 \text{ km}$. Computing the moment magnitude for this event roughly leads to $M_W < 2.1$. Thereby, an average slip of 2 m and a shear modulus of $\sim 65.9 \text{ GPa}$ are assumed. The magnitude of the simulated earthquake strongly differs from the real observations of the Mojabana event ($M_W 6.5$). This is not remarkable as it reinforces the fact that the inferred fault plane is not suitable.

4 Simulation of the Rupture Dynamics

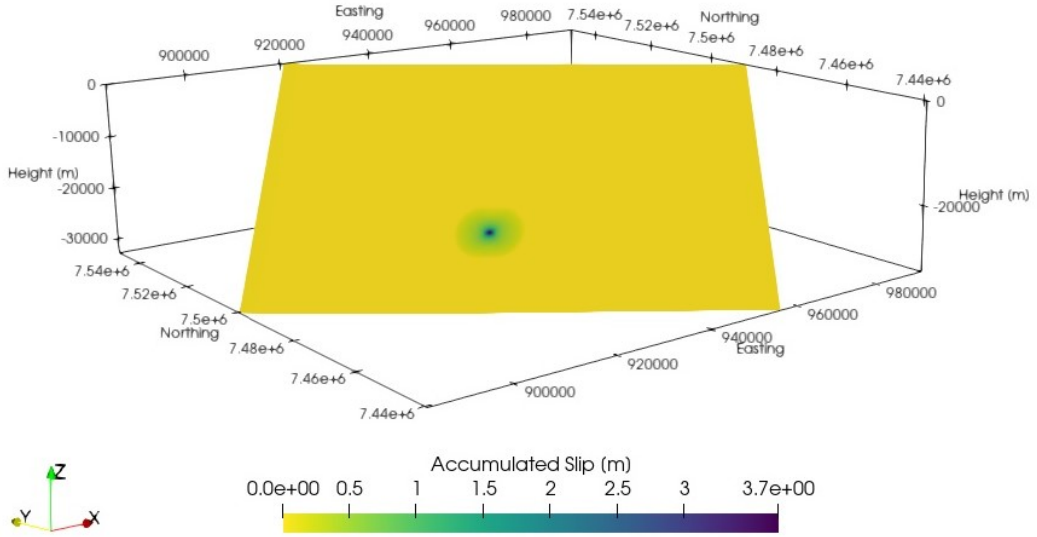


Figure 13: Accumulated slip on the fault. The slip achieves its maximum at the hypocenter. The rupture is constrained by a small area. Orientation of the axes: $x \equiv$ east, $y \equiv$ north, $z \equiv$ height.

Free Surface Output

SeisSol produces free surface output such as ground velocities and ground displacements. In our model the fault is buried in depth. Despite the overlying sediments, the simulation reveals a deformation on the surface. We obtain horizontal displacements in both x - and y -directions and a vertical displacement along the z -axis. They are depicted in Figure 14. The maximum horizontal displacements along the x - and y -axes are -2.7 cm and -2.8 cm, respectively. In total, the vertical z -axis reveals the highest deformation of -4.3 cm (Figure 14c). This seems reasonable because we set up the simulation with $\nu = 0.5$ and the principal stress axis σ_1 being vertical: $S_V = 1$. Thus, the simulated earthquake should promote normal faulting which apparently results in a subsidence of the closest epicentral area. The simulation was set up for the second fault plane which dips to southwest. However, these findings are better explained with a causative fault plane dipping to northeast. This may further indicate, that the first fault plane (dip of 73° to NE) is more suitable to explain the Mojabana earthquake.

4.3 Results and Discussion

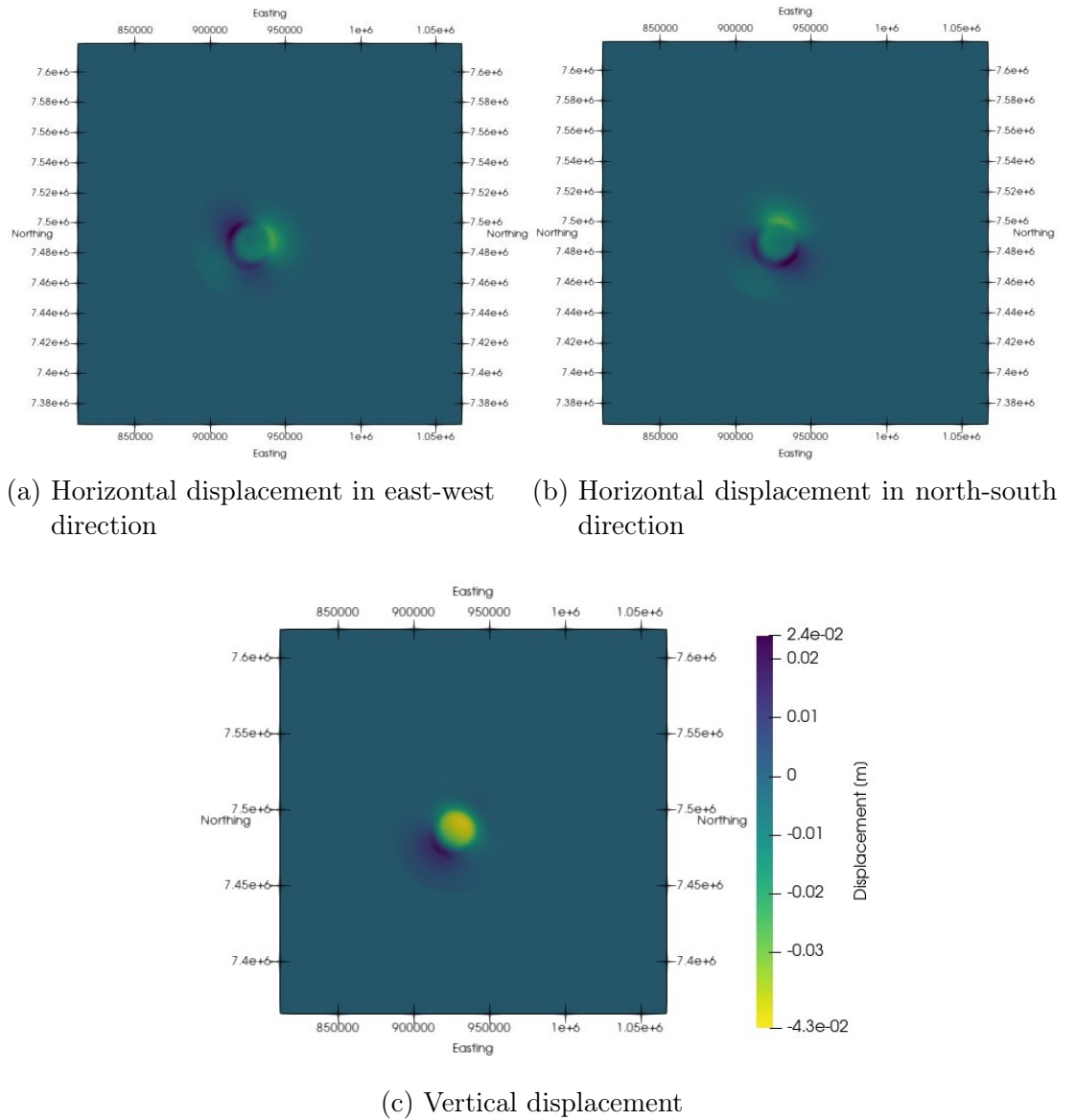


Figure 14: Ground deformation on the free surface. The simulation reveals a displacement in horizontal and vertical directions. North points to the top.

5 Conclusion and Outlook

This thesis focuses on the large M_W 6.5 Mojabana intraplate earthquake in Botswana. At plate boundaries, the knowledge of seismic energy release in form of recurring earthquakes is comparably good. In contrast, earthquakes within plate interiors are quite rare. As opportunities to study them are limited, their understanding is still poor. Since the Mojabana event is the largest intraplate earthquake in the last 30 years and detailed geophysical data is available, it poses an unique chance to gain new insights in these poorly understood phenomenons. Several authors previously evaluated causative fault planes that might be the source of the Mojabana earthquake (Table 1). Because of remaining discrepancies regarding its trigger mechanism, this thesis elaborates a new fault plane solution to explain its origin. Knowing that the Global Centroid Moment Tensor provides two admissible solutions for this event, there are exactly two fault planes that can cause the Mojabana earthquake. A first fault plane solution was proposed by Obermaier [2020]. Using the same data sets, we try to give an estimate on the second fault plane solution.

To pursue this goal, we visualize the hypocenter of the main event, its aftershocks, the resistivity distribution from a magneto-telluric model, and the first fault plane solution as three-dimensional model in the visualization software Paraview (Figure 5 and Figure 6). Taking account of a normal faulting focal mechanism and abrupt changes in the resistivity model, we can cut down on the orientation of the second fault plane. We find a planar fault plane that strikes northwest-southeast with 126° and dips to southwest at 28°.

Assessing the validity of the inferred fault plane, we need to constrain its static strength. Therefore, we perform static analysis on the fault plane. We account for the frictional behaviour of the fault, its lithologic vicinity, and the state of stress (Table 2). Under the assumption of an Andersonian stress regime, we only need four parameters to fully characterize the fault's stress state. We constrain

5 Conclusion and Outlook

the parameter range of these quantities, namely the stress shape ratio ν , the fluid pressure ratio γ , the initial relative prestress ratio R_0 , and the azimuth of maximum horizontal compressive stress S_{Hmax} . Taking these values together, we plot the distribution of the normalized relative prestress ratio on the fault plane. This $\frac{R}{R_0}$ -ratio describes the closeness of the fault to failure. The higher its value, the more likely the fault ruptures into an earthquake.

All observations of the Moijabana earthquake confirm an extensional normal faulting mechanism. Consequently, there is no need to challenge the value of the stress shape ratio, as $\nu = 0.5$ describes a purely extensional faulting regime. Yet, there is no evidence on the presence of fluids in the vicinity of the Moijabana earthquake. Therefore, we have to constrain the parameter range of the fluid pressure ratio by trial and error. We increase this quantity from hydrostatic ($\gamma = 0.37$) to lithostatic conditions. However, calculating the normalized relative prestress ratio for each γ -value (Table 3) and comparing the results does not reveal any variations in the output. This is interesting, as Equation 6 implies a large contribution of the fluid pressure ratio to the observed stress drop. Hence, it strongly controls the size of the simulated earthquake. In order to better compare the output of the subsequent dynamic rupture simulations with previous results from Obermaier [2020], we set the fluid pressure ratio to $\gamma = 0.95$.

The parameter space of the initial relative prestress ratio is varied between 0.2–1.0 in steps of 0.1 since the value of this quantity is completely unknown. The distribution of the normalized relative prestress ratio for varied R_0 -values shows that $R_0 = 0.3$ maintains the maximum (Figure 8).

Values for the azimuth of maximum horizontal compressive stress can be constrained by observations. Because of their bad quality in the nearest surroundings of the epicenter (Table 4), S_{Hmax} is varied from 102° – 182° . As expected, S_{Hmax} strongly influences the state of stress on the fault (Figure 9). Our findings reveal a value of $S_{Hmax} = 134^\circ$ to be most suitable as it maximizes the normalized relative prestress ratio. This value matches roughly the general observations of the World Stress Map.

In summary, we find that the combination of $\nu = 0.5$, $\gamma = 0.95$, $R_0 = 0.3$, and $S_{Hmax} = 134^\circ$ maximizes the normalized relative prestress ratio on our fault. Nevertheless, our fault is far from critical loading ($R \approx R_0$). Consequently, we do not expect rupture to nucleate. Furthermore, this $\frac{R}{R_0}$ -ratio is comparably low

when we evaluate static analysis results of the first fault plane. In direct comparison of Figure 10 and Figure 11 it becomes obvious that the fault geometry has a significant influence on the static strength of the fault. Herein, the normalized relative prestress ratio is calculated with the same initial conditions ($\nu = 0.5$, $\gamma = 0.95$, $R_0 = 0.7$, $S_{Hmax} = 132^\circ$) and its distribution is plotted on the two different fault geometries. These initial conditions were ascertained by Obermaier [2020]. The first fault plane consistently shows higher $\frac{R}{R_0}$ -ratios than the second fault plane. We conclude that the second fault plane might not be suitable to host a large M_W 6.5 earthquake as it happened in Botswana. Hereupon, a small change in stress would probably not nucleate an earthquake, unlike it could be the case for the first fault plane.

To verify the overhead considerations, we run dynamic rupture simulations on the supercomputer SuperMUC in Garching, near Munich. The modeling setup consists of discretizing our model domain (Figure 12) and input files accounting for material properties, stress conditions, and friction law parameters (Table 5). The first simulation with the constrained parameters confirms the assumption that an earthquake might not nucleate on the second fault plane. After 1.3 s the simulation is aborted. Because of the too low background stress, rupture does not start.

We run a second simulation with the initial parameters ascertained by Obermaier [2020]. It becomes clear that this setup does not lead to nucleation either. To nucleate, we increase the relative prestress ratio in the nucleation area and reduce the effective confining stress. Hereby, we obtain a 2.3 s long rupture across an area of approximately 10 km \times 10 km (Figure 13). The simulated earthquake shows a magnitude $M_W < 2.1$. It strongly differs from previous results for the Mojabana earthquake (Table 1), which is not unexpected as it confirms the notion that the second fault plane is not suitable. The free surface output indicates an extensional regime (Figure 14). This is compatible with the vertical principal stress axis σ_1 . These findings should be compared with previous results to verify our model. However, the initial parameters of our simulated earthquake are rather artificial and would not correspond to nature. Therefore, comparison and evaluation of different outcomes may not be meaningful.

The objective of this thesis – namely the evaluation of a trigger mechanism for the Mojabana earthquake – could not be met entirely. Since our model does not

5 Conclusion and Outlook

fulfill the necessary criterions for a realistic earthquake, comparing our findings with previous results, such as the inversion of InSAR data, is not meaningful. Nevertheless, we can conclude that the inferred fault plane is not the causative fault plane for the Mojabana event. Although we have detailed geophysical data available, all results imply uncertainties as they are based on geophysical models and rough estimations. For instance, the exact location of the second fault plane was inferred by abrupt changes in the magneto-telluric model. Figure 7 considers two possible fault traces for the second fault plane. We chose the orange trace as it fits best but the blue trace would probably be suited equally well. Performing static analysis on the fault plane of the blue trace is advised for validation. In addition, further investigations are strongly required in order to gain a better understanding of our model. For instance, constraining the influence of the fluid pressure ratio on dynamic rupture is essential. Additionally, more simulations with broadly varying conditions from hydrostatic to lithostatic should be performed. Due to the limited time, they could not be carried forward in this thesis. Furthermore, friction law parameters from previous projects in different geologic settings were applied to our model (Table 5). They therefore include deviations and lead to uncertainties in our results. Hence, it is recommended to constrain these quantities for the setting of the Mojabana earthquake in Botswana. If all these improvements are carried out, a better understanding of intraplate events regarding their genesis and impacts is certain. Consequently, hazard calculations could be improved in order to prevent earthquake damages in infrastructures and especially to save human lives.

List of Figures

1	Worldwide seismic activity of intraplate earthquakes	2
2	Map of southern Africa	6
3	Seismicity of Botswana	8
4	Tectonic map of Botswana	10
5	Visualization of both first and second fault plane	15
6	Visualization of the conductivity	16
7	Location of the fault traces	17
8	Normalized distribution of R under variation of R_0	25
9	Normalized distribution of R under variation of S_{Hmax} for $R_0 = 0.3$.	26
10	Normalized distribution of R on the first fault plane under variation of S_{Hmax}	28
11	Normalized distribution of R on the second fault plane under variation of S_{Hmax}	30
12	Visualization of the generated mesh	33
13	Accumulated slip on the fault	36
14	Ground deformation on the free surface	37

List of Tables

1	Fault plane parameters	7
2	Applied parameters for the calculation of R	19
3	Variation of ρt	21
4	Values of S_{Hmax} from the World Stress Map	23
5	Dynamic rupture friction parameters	34

Bibliography

- Albano, M., Polcari, M., Bignami, C., Moro, M., Saroli, M., & Stramondo, S. (2017). Did Anthropogenic Activities Trigger the 3 April 2017 Mw 6.5 Botswana Earthquake? *Remote Sensing*, 9(10). <https://doi.org/10.3390/rs9101028>
- Aochi, H., & Madariaga, R. (2003). The 1999 Izmit, Turkey, Earthquake: Non-planar Fault Structure, Dynamic Rupture Process, and Strong Ground Motion. *Bulletin of the Seismological Society of America*, 93(3), 1249–1266. <https://doi.org/10.1785/0120020167>
- Bettinelli, P., Avouac, J.-P., Flouzat, M., Bollinger, L., Ramillien, G., Rajaure, S., & Sapkota, S. (2008). Seasonal variations of seismicity and geodetic strain in the Himalaya induced by surface hydrology. *Earth and Planetary Science Letters*, 266(3), 332–344. <https://doi.org/10.1016/j.epsl.2007.11.021>
- Bird, P. (2003). An updated digital model of plate boundaries. *Geochemistry, Geophysics, Geosystems*, 4(3). <https://doi.org/10.1029/2001GC000252>
- Botswana Geoscience Institute. (2018). *Annual Report 2018* (technical report). Botswana Geoscience Institute. Private Bag 0014, Plot 11566, Khama Avenue 1, Lobatse, Botswana.
- Bowman, J. R. (1992). The 1988 Tennant Creek, northern territory, earthquakes: A synthesis. *Australian Journal of Earth Sciences*, 39(5), 651–669. <https://doi.org/10.1080/08120099208728056>
- Bufford, K. M., Atekwana, E. A., Abdelsalam, M. G., Shemang, E., Atekwana, E. A., Mickus, K., Moidaki, M., Modisi, M. P., & Molwalefhe, L. (2012). Geometry and faults tectonic activity of the Okavango Rift Zone, Botswana: Evidence from magnetotelluric and electrical resistivity tomography imaging. *Journal of African Earth Sciences*, 65, 61–71. <https://doi.org/10.1016/j.jafrearsci.2012.01.004>

Bibliography

- Calais, E., Camelbeeck, T., Stein, S., Liu, M., & Craig, T. J. (2016). A new paradigm for large earthquakes in stable continental plate interiors. *Geophysical Research Letters*, 43(20), 10.621–10.637. <https://doi.org/10.1002/2016GL070815>
- Calais, E., Freed, A. M., Arsdale, R. V., & Stein, S. (2010). Triggering of New Madrid seismicity by late-Pleistocene erosion. *Nature*, 466(7306), 608–611. <https://doi.org/10.1038/nature09258>
- Cappa, F., Rutqvist, J., & Yamamoto, K. (2009). Modeling crustal deformation and rupture processes related to upwelling of deep CO₂-rich fluids during the 1965–1967 Matsushiro earthquake swarm in Japan. *Journal of Geophysical Research: Solid Earth*, 114(B10). <https://doi.org/10.1029/2009JB006398>
- CartoGIS Services, College of Asia and the Pacific, & The Australian National University. (2021). *Southern Africa*. Retrieved March 24, 2021, from <http://asiapacific.anu.edu.au/mapsonline/base-maps/southern-africa>
- Chisenga, C., van der Meijde, M., Yan, J., Fadel, I., Atekwana, E. A., Steffen, R., & Ramotoroko, C. (2020). Gravity derived crustal thickness model of Botswana: Its implication for the Mw 6.5 April 3, 2017, Botswana earthquake. *Tectonophysics*, 787, 228479. <https://doi.org/10.1016/j.tecto.2020.228479>
- Clark, D., McPherson, A., & Dissen, R. V. (2012). Long-term behaviour of Australian stable continental region (SCR) faults. *Tectonophysics*, 566-567, 1–30. <https://doi.org/10.1016/j.tecto.2012.07.004>
- Fadel, I., Paulssen, H., van der Meijde, M., Kwadiba, M., Ntibinyane, O., Nyblade, A., & Durrheim, R. (2020). Crustal and Upper Mantle Shear Wave Velocity Structure of Botswana: The 3 April 2017 Central Botswana Earthquake Linked to the East African Rift System. *Geophysical Research Letters*, 47(4). <https://doi.org/10.1029/2019GL085598>
- Fadel, I., van der Meijde, M., & Paulssen, H. (2018). Crustal Structure and Dynamics of Botswana. *Journal of Geophysical Research: Solid Earth*, 123(12), 10, 659–10, 671. <https://doi.org/10.1029/2018JB016190>
- Gabriel, A.-A., Ulrich, T., Li, D., Uphoff, C., Taufiqurrahman, T., & Wirp, S. A. (2021). *SeisSol - High Resolution Simulation of Seismic Wave Propagation in Realistic Media with Complex Geometry*. Retrieved April 21, 2021, from <https://www.seissol.org/>

Bibliography

- Gardonio, B., Jolivet, R., Calais, E., & Leclère, H. (2018). The April 2017 Mw 6.5 Botswana Earthquake: An Intraplate Event Triggered by Deep Fluids. *Geophysical Research Letters*, 45(17), 8886–8896. <https://doi.org/10.1029/2018GL078297>
- González, P. J., Tiampo, K. F., Palano, M., Cannavó, F., & Fernández, J. (2012). The 2011 Lorca earthquake slip distribution controlled by groundwater crustal unloading. *Nature Geoscience*, 5(11), 821–825. <https://doi.org/10.1038/ngeo1610>
- Gupta, H. K. (1985). The present status of reservoir induced seismicity investigations with special emphasis on Koyna earthquakes [Quantification of Earthquake]. *Tectonophysics*, 118(3), 257–279. [https://doi.org/10.1016/0040-1951\(85\)90125-8](https://doi.org/10.1016/0040-1951(85)90125-8)
- Hanks, T. C., & Johnston, A. C. (1992). Common features of the excitation and propagation of strong ground motion for North American earthquakes. *Bulletin of the Seismological Society of America*, 82(1), 1–23.
- Heidbach, O., Rajabi, M., Reiter, K., & Ziegler, M. (2016a). World Stress Map 2016 [GFZ Data Services]. <https://doi.org/10.5880/WSM.2016.002>
- Heidbach, O., Rajabi, M., Reiter, K., Ziegler, M., & WSM Team. (2016b). World Stress Map Database Release 2016 [V. 1.1. GFZ Data Services]. <https://doi.org/10.5880/WSM.2016.001>
- Heki, K. (2003). Snow load and seasonal variation of earthquake occurrence in Japan. *Earth and Planetary Science Letters*, 207(1), 159–164. [https://doi.org/10.1016/S0012-821X\(02\)01148-2](https://doi.org/10.1016/S0012-821X(02)01148-2)
- Hetzel, R., & Hampel, A. (2005). Slip rate variations on normal faults during glacial–interglacial changes in surface loads. *Nature*, 435(7038), 81–84. <https://doi.org/10.1038/nature03562>
- Hough, S. E., Armbruster, J. G., Seeber, L., & Hough, J. F. (2000). On the Modified Mercalli intensities and magnitudes of the 1811–1812 New Madrid earthquakes. *Journal of Geophysical Research: Solid Earth*, 105(B10), 23,839–23,846. <https://doi.org/10.1029/2000JB900110>
- Johnston, A. C. (1989). The Seismicity of ‘Stable Continental Interiors’ [NATO ASI Series (Series C: Mathematical and Physical Sciences)]. In S. Gregersen & P. W. Basham (Editors), *Earthquakes at North-Atlantic Passive Margins: Neotectonics and Postglacial Rebound* (Pages 299–327). Springer Netherlands. https://doi.org/10.1007/978-94-009-2311-9_18

Bibliography

- Kachingwe, M., Nyblade, A., & Julià, J. (2015). Crustal structure of Precambrian terranes in the southern African subcontinent with implications for secular variation in crustal genesis. *Geophysical Journal International*, 202(1), 533–547. <https://doi.org/10.1093/gji/ggv136>
- Kamenetsky, V. S., Golovin, A. V., Maas, R., Giuliani, A., Kamenetsky, M. B., & Weiss, Y. (2014). Towards a new model for kimberlite petrogenesis: Evidence from unaltered kimberlites and mantle minerals. *Earth-Science Reviews*, 139, 145–167. <https://doi.org/10.1016/j.earscirev.2014.09.004>
- Keranen, K. M., Weingarten, M., Abers, G. A., Bekins, B. A., & Ge, S. (2014). Sharp increase in central Oklahoma seismicity since 2008 induced by massive wastewater injection. *American Association for the Advancement of Science*, 345(6195), 448–451. <https://doi.org/10.1126/science.1255802>
- Kolawole, F., Atekwana, E. A., Malloy, S., Stamps, D. S., Grandin, R., Abdelsalam, M. G., Leseane, K., & Shemang, E. M. (2017). Aeromagnetic, gravity, and Differential Interferometric Synthetic Aperture Radar analyses reveal the causative fault of the 3 April 2017 Mw 6.5 Moiyabana, Botswana, earthquake. *Geophysical Research Letters*, 44(17), 8837–8846. <https://doi.org/10.1002/2017GL074620>
- Leseane, K., Atekwana, E., Mickus, K., Abdelsalam, M., Shemang, E., & Atekwana, E. (2015). Thermal perturbations beneath the incipient Okavango Rift Zone, Northwest Botswana. *Journal of Geophysical Research: Solid Earth*, 120. <https://doi.org/10.1002/2014JB011029>
- Long, L. T. (1976). Speculations Concerning Southeastern Earthquakes, Mafic Intrusions, Gravity Anomalies and Stress Amplification. *Seismological Research Letters*, 47(3), 29–35. <https://doi.org/10.1785/gssrl.47.3.29>
- Materna, K., Wei, S., Wang, X., Heng, L., Wang, T., Chen, W., Salman, R., & Bürgmann, R. (2019). Source characteristics of the 2017 Mw6.4 Moijabana, Botswana earthquake, a rare lower-crustal event within an ancient zone of weakness. *Earth and Planetary Science Letters*, 506, 348–359. <https://doi.org/10.1016/j.epsl.2018.11.007>
- Mazzotti, S. (2007). Geodynamic models for earthquake studies in intraplate North America. *Continental intraplate earthquakes: Science, hazard, and policy issues*. Geological Society of America. [https://doi.org/10.1130/2007.2425\(02\)](https://doi.org/10.1130/2007.2425(02))

Bibliography

- Midzi, V., Saunders, I., Manzunzu, B., Kwadiba, M. T., Jele, V., Mantsha, R., Marimira, K. T., Mulabisana, T. F., Ntibinyane, O., Pule, T., Rathod, G. W., Sitali, M., Tabane, L., van Aswegen, G., & Zulu, B. S. (2018). The 03 April 2017 Botswana M6.5 earthquake: Preliminary results. *Journal of African Earth Sciences*, 143, 187–194. <https://doi.org/10.1016/j.jafrearsci.2018.03.027>
- Modisi, M. P., Atekwana, E. A., Kampunzu, A. B., & Ngwisanzi, T. H. (2000). Rift kinematics during the incipient stages of continental extension: Evidence from the nascent Okavango rift basin, northwest Botswana. *Geology*, 28(10), 939–942. [https://doi.org/10.1130/0091-7613\(2000\)28<939:RKDTIS>2.0.CO;2](https://doi.org/10.1130/0091-7613(2000)28<939:RKDTIS>2.0.CO;2)
- Mooney, W. D., Ritsema, J., & Hwang, Y. K. (2012). Crustal seismicity and the earthquake catalog maximum moment magnitude (Mcmax) in stable continental regions (SCRs): Correlation with the seismic velocity of the lithosphere. *Earth and Planetary Science Letters*, 357-358, 78–83. <https://doi.org/10.1016/j.epsl.2012.08.032>
- Moorkamp, M., Atekwana, E., Fadel, I., Gabriel, A.-A., Kolawole, F., Shemang, E., Ramotoroko, C., van der Meijde, M., Mickus, K., Selepong, A., & Molwalefhe, L. (2020). Integrated geophysical analysis of the April 2017 Moiyabana intra-plate earthquake, Botswana [Online, 4–8 May 2020]. *EGU General Assembly Conference Abstracts*. <https://doi.org/10.5194/egusphere-egu2020-9241>
- Moorkamp, M., Fishwick, S., Walker, R. J., & Jones, A. G. (2019). Geophysical evidence for crustal and mantle weak zones controlling intra-plate seismicity – the 2017 Botswana earthquake sequence. *Earth and Planetary Science Letters*, 506, 175–183. <https://doi.org/10.1016/j.epsl.2018.10.048>
- Obermaier, T. (2020). *Mechanisms of intraplate earthquakes: The 2017 Botswana event* (Bachelor's Thesis). Ludwig-Maximilians-Universität München and Technische Universität München. München.
- Olebetse, T. A., Mmese, M. L., Simon, R. E., & Maritinkole, J. (2020). Some Foreshocks and Aftershocks Associated with the Moiyabana Earthquake of 2017 in Botswana. *International Journal of Geosciences*, 11, 238–250. <https://doi.org/10.4236/ijg.2020.114013>
- Pagani, M., Garcia-Pelaez, J., Gee, R., Johnson, K., Poggi, V., Styron, R., Weatherill, G., Simionato, M., Viganò, D., Danciu, L., & Monelli, D. (2018).

Bibliography

- Global Earthquake Model (GEM) Seismic Hazard Map [Version 2018.1 - December 2018]. <https://doi.org/10.13117/GEM-GLOBAL-SEISMIC-HAZARD-MAP-2018.1>
- Palgunadi, K. H., Gabriel, A.-A., Ulrich, T., Lopéz-Comino, J.-Á., & Mai, P. M. (2020). Dynamic Fault Interaction during a Fluid-Injection-Induced Earthquake: The 2017 Mw 5.5 Pohang Event. *Bulletin of the Seismological Society of America*. <https://doi.org/10.1785/0120200106>
- Ramotoroko, C., Ranganai, R., & Nyabeze, P. (2016). Extension of the Archaean Madibe-Kraaipan granite-greenstone terrane in southeast Botswana: Constraints from gravity and magnetic data. *Journal of African Earth Sciences*, 123, 39–56. <https://doi.org/10.1016/j.jafrearsci.2016.06.016>
- Ranganai, R. T., Kampunzu, A. B., Atekwana, E. A., Paya, B. K., King, J. G., Koosimile, D. I., & Stettler, E. H. (2002). Gravity evidence for a larger Limpopo Belt in southern Africa and geodynamic implications. *Geophysical Journal International*, 149(3), F9–F14. <https://doi.org/10.1046/j.1365-246X.2002.01703.x>
- Russell, J. K., Porritt, L. A., Lavallée, Y., & Dingwell, D. B. (2012). Kimberlite ascent by assimilation-fuelled buoyancy. *Nature*, 481(7381), 352–356. <https://doi.org/10.1038/nature10740>
- Stamps, D. S., Calais, E., Saria, E., Hartnady, C., Nocquet, J.-M., Ebinger, C. J., & Fernandes, R. M. (2008). A kinematic model for the East African Rift. *Geophysical Research Letters*, 35(5). <https://doi.org/10.1029/2007GL032781>
- Sykes, L. R. (1978). Intraplate seismicity, reactivation of preexisting zones of weakness, alkaline magmatism, and other tectonism postdating continental fragmentation. *Reviews of Geophysics*, 16(4), 621–688. <https://doi.org/10.1029/RG016i004p00621>
- Talwani, P. (1988). The Intersection Model for Intraplate Earthquakes. *Seismological Research Letters*, 59(4), 305–310. <https://doi.org/10.1785/gssrl.59.4.305>
- Talwani, P. (2014). Unified model for intraplate earthquakes. In P. Talwani (Editor), *Intraplate Earthquakes* (Pages 275–302). Cambridge University Press.
- Talwani, P. (2017). On the nature of intraplate earthquakes. *Journal of Seismology*, 21(1), 47–68. <https://doi.org/10.1007/s10950-016-9582-8>

Bibliography

- The SeisSol Team Revision. (2021). *Meshing with SimModeler*. Retrieved April 22, 2021, from <https://seissol.readthedocs.io/en/latest/meshing-with-simmodeler.html>
- Turpeinen, H., Hampel, A., Karow, T., & Maniatis, G. (2008). Effect of ice sheet growth and melting on the slip evolution of thrust faults. *Earth and Planetary Science Letters*, 269(1), 230–241. <https://doi.org/10.1016/j.epsl.2008.02.017>
- Ulrich, T., Vater, S., Madden, E. H., Behrens, J., van Dinther, Y., van Zelst, I., Fielding, E. J., Liang, C., & Gabriel, A.-A. (2019a). Coupled, Physics-Based Modeling Reveals Earthquake Displacements are Critical to the 2018 Palu, Sulawesi Tsunami. *Pure and Applied Geophysics*, 176(10), 4069–4109. <https://doi.org/10.1007/s0024-019-02290-5>
- Ulrich, T., Gabriel, A.-A., Ampuero, J.-P., & Xu, W. (2019b). Dynamic viability of the 2016 Mw 7.8 Kaikōura earthquake cascade on weak crustal faults. *Nature Communications*, 10(1213). <https://doi.org/10.1038/s41467-019-09125-w>
- U.S. Geological Survey. (2021). *Earthquake Hazards Program*. Retrieved March 24, 2021, from <https://earthquake.usgs.gov/>
- Yadav, R. K., Kundu, B., Gahalaut, K., Catherine, J., Gahalaut, V. K., Ambikapthy, A., & Naidu, M. S. (2013). Coseismic offsets due to the 11 April 2012 Indian Ocean earthquakes (Mw 8.6 and 8.2) derived from GPS measurements. *Geophysical Research Letters*, 40(13), 3389–3393. <https://doi.org/10.1002/grl.50601>
- Zoback, M. L. (1992). First- and second-order patterns of stress in the lithosphere: The World Stress Map Project. *Journal of Geophysical Research: Solid Earth*, 97(B8), 11703–11728. <https://doi.org/10.1029/92JB00132>
- Zoback, M. L., & Richardson, R. M. (1996). Stress perturbation associated with the Amazonas and other ancient continental rifts. *Journal of Geophysical Research: Solid Earth*, 101(B3), 5459–5475. <https://doi.org/10.1029/95JB03256>

Statement of Authorship

I hereby declare that this thesis submitted is my own unaided work. I did not use any other than the stated resources and all direct or indirect sources are acknowledged in the bibliography. This thesis has not previously been presented to another examination board and has not been published in this or any other version.

Munich, May 3, 2021

Sophia Gahr